SANDIA REPORT

SAND2014-19513
Unlimited Release
Printed October 2014

Ultrafast Laser Diagnostics for Energetic-Material Ignition Mechanisms: Tools for Physics-Based Model Development

Brook A. Jilek, Ian T. Kohl , Darcie A. Farrow, Junji Urayama, and Sean P. Kearney

Prepared by
Sandia National Laboratories
Albuquerque, New Mexico 87185 and Livermore, California 94550

Sandia National Laboratories is a multi-program laboratory managed and operated by Sandia Corporation,
a wholly owned subsidiary of Lockheed Martin Corporation, for the U.S. Department of Energy's
National Nuclear Security Administration under contract DE-AC04-94AL85000.

Issued by Sandia National Laboratories, operated for the United States Department of Energy by Sandia Corporation.

Available to DOE and DOE contractors from
U.S. Department of Energy
Office of Scientific and Technical Information
P.O. Box 62
Oak Ridge, TN 37831

Telephone: (865) 576-8401
Facsimile: (865) 576-5728
E-Mail: reports@adonis.osti.gov
Online ordering: http://www.osti.gov/bridge

Available to the public from
U.S. Department of Commerce
National Technical Information Service
5285 Port Royal Rd.
Springfield, VA 22161

Telephone: (800) 553-6847
Facsimile: (703) 605-6900
E-Mail: orders@ntis.fedworld.gov
Online order: http://www.ntis.gov/help/ordermethods.asp?loc=7-4-0#online

SAND2014-19513
Unlimited Release
Printed October 2014

Ultrafast Laser Diagnostics for Energetic-Material Ignition Mechanisms: Tools for Physics-Based Model Development

Brook A. Jilek, Ian T. Kohl, Darcie A. Farrow
Energetic Materials Dynamic and Reactive Science Department 2554

Junji Urayama
Laser Applications Department 5444

Sean P. Kearney
Thermal/Fluid Experimental Sciences Department 1512

Sandia National Laboratories
P.O. Box 5800
Albuquerque, New Mexico 87185

Abstract

We present the results of an LDRD project to develop diagnostics to perform fundamental measurements of material properties during shock compression of condensed phase materials at micron spatial scales and picosecond time scales. The report is structured into three main chapters, which each focus on a different diagnostic development effort. Direct picosecond laser drive is used to introduce shock waves into thin films of energetic and inert materials. The resulting laser-driven shock properties are probed via Ultrafast Time Domain Interferometry (UTDI), which can additionally be used to generate shock Hugoniot data in tabletop experiments. Stimulated Raman scattering (SRS) is developed as a temperature diagnostic. A transient absorption spectroscopy setup has been developed to probe shock-induced changes during shock compression. UTDI results are presented under dynamic, direct-laser-drive conditions and shock Hugoniots are estimated for inert polystyrene samples and for the explosive hexanitroazobenzene, with results from both Sandia and Lawrence Livermore presented here. SRS and transient absorption diagnostics are demonstrated on static thin-film samples, and paths forward to dynamic experiments are presented.

ACKNOWLEDGMENTS

We would like to gratefully acknowledge Mike Armstrong and Joe Zaug of Lawrence Livermore National Laboratory for their ample help in getting the Ultrafast Time Domain Interferometry experiment started and for collaborating with us on Hugoniot measurements of hexanitroazobenzene (HNAB). They provided us with their Mathematica and Matlab analysis routines that served as a basis for our own Matlab code. They also provided invaluable experimental advice along the way as difficulties arose. We thank Shawn McGrane, Cindy Bolme, Katie Brown, and David Moore at Los Alamos National Laboratory for their advice and encouragement. We also thank Alex Tappan, Rob Knepper and Michael Marques at Sandia National Laboratories (Org. 2554) for making the vapor-deposited samples used throughout this work. The help of Gregg Radtke inn constructing a least-squares optimization routine to fit UTDI data is greatly appreciated.

Sandia is a multiprogram laboratory operated by Sandia Corporation, a Lockheed-Martin Company, for the United States Department of Energy's National Nuclear Security Administration under Contract DE-AC04-94AL85000.

CONTENTS

FIGURES

TABLES

1. INTRODUCTION

Despite its importance, a fundamental description of initiation in energetic materials has eluded researchers for decades, in large part because ignition results from mechanical and thermochemical mechanisms that are tightly coupled at extreme spatial and temporal scales of order microns and picoseconds. Access to these extreme time and length scales under dynamic loading conditions has, until recently, been restricted to simulations, and experiments to underpin the relevant physics are sorely needed to provide model developers with an appropriate physical foundation. The recent availability of femtosecond laser sources has opened the door to fundamental experiments with the required extreme resolution, and well-controlled measurements on the early time effects of shock drive are now possible.

This project represents a development effort to cultivate state-of-the-art tabletop diagnostic tools for probing of energetic materials under dynamic shock loading. Efforts are focused on thin films of both inert and energetic materials, which makes the experiments amenable to direct laser-driven generation of shock waves and results in experimental conditions which are free of many of personnel hazards associated with explosive operations. The report is centered around three primary diagnostic-development efforts, each of which is highlighted independently in its own chapter. Chapter 2 of this report is devoted to Ultrafast Time-Domain Interferometry (UTDI) as well as methods for utilizing shaped picosecond laser pulses to impart shock drive into the thin-film samples. UTDI is important because it characterizes the mechanical and shock response of the film to the laser drive, providing shock characterization and boundary conditions for any spectroscopic measurement of the material response. UTDI provides the additional advantage of yielding shock Hugoniot data for materials, enabling tabletop Hugoniot measurement capability. Chapter 3 is focused on the application of stimulated Raman scattering (SRS) for thermometry. Temperature has proven to be a particularly difficult parameter to measure in dynamic experiments. The SRS capability developed here has been demonstrated with two different laser schemes, and results on static films are reported here. Chapter 4 concludes this report and is dedicated to the development of ultra-broadband absorption spectroscopy schemes for characterization of explosive samples.

2. ULTRAFAST TIME DOMAIN INTERFEROMETY (UTDI)

2.1 UTDI Experimental Setup

Here we have implemented a laser-based tabletop diagnostic, Ultrafast Time Domain Interferometry (UTDI), originally developed by Benuzzi-Mounaix [1], recently refined by Armstrong, *et al.* at Lawrence Livermore National Laboratory [2], and closely related to work by Bolme, *et al.*, at Los Alamos National Laboratory [3]. The method enables high-throughput measurements of Hugoniot data for a wide variety of materials including high explosives (HEs). UTDI overcomes time-resolution limitations of other diagnostics such as Photon Doppler Velocimetry (PDV) and Velocity Interferometry System for Any Reflector (VISAR) by encoding temporal information within the spectrum of a probe pulse.

A conceptual diagram of the experimental setup is provided in [2]. A broadband (25 nm full-width at half-max FWHM) femtosecond pulse is chirped so that the various wavelengths travel different path lengths and become more separated in time, resulting in a probe pulse that is 300 or more picoseconds (FWHM) in duration. One edge of a laser pulse is clipped in the beam stretcher to produce a ~ 25 ps rise-time profile. This chirped pulse is split into two portions: a higher energy pulse to generate a shock within a target and a low-energy pulse that propagates through a Michelson interferometer to form a pulse-pair with a relative time separation of ~10-15 ps. The drive pulse is focused down to a ~ 20-30 μm spot on the substrate side of an aluminum target; rapid ionization within the skin-depth of the aluminum ablator impulsively launches a shock wave that travels through the Al and into a sample material that is deposited onto the back side of the ablator surface. On the backside of the ablator, the probe pulses are focused to a ~ 100 μm spot to illuminate the entire shock break-out area, including unshocked reference regions beyond the periphery of the drive pulse spot. An objective lens is selected to image the surface of the sample onto the slit of an imaging spectrometer. A CCD camera attached to the spectrometer records an interference pattern created by the relative path-length differences between corresponding wavelengths in the probe pulse pair.

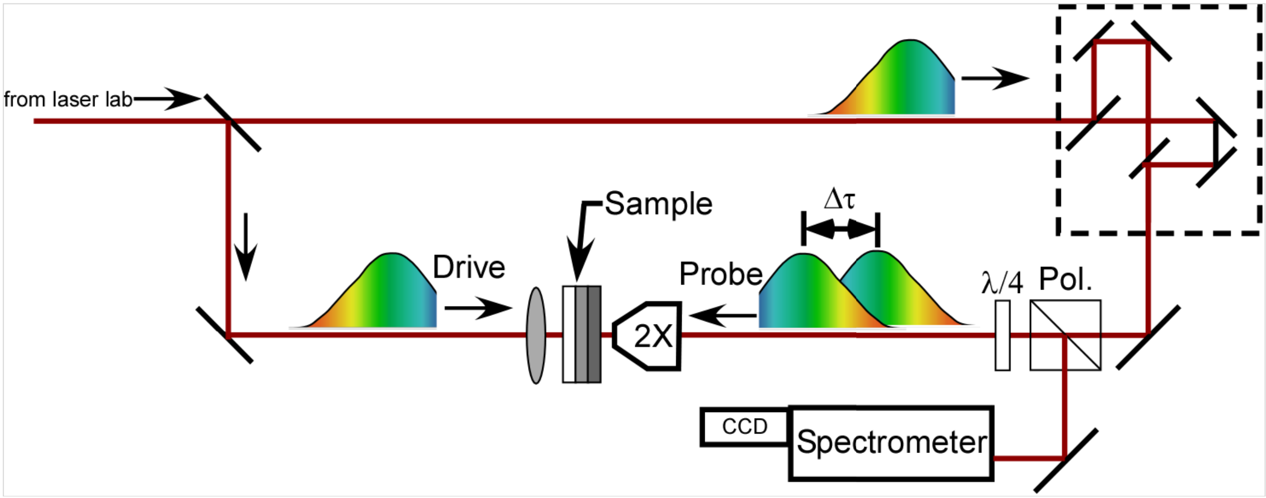

Figure 1 Essential elements of the UTDI experimental system.

Extreme, picosecond-scale time resolution is achieved in UTDI measurements by encoding time information into the frequency domain via the above-mentioned temporal chirp in the stretched laser pulse. The structure of a typical chirped pulse is shown in Fig. 2. At left in Fig. 2 is as second-harmonic FROG (Frequency Resolved Optical Gate) trace, which displays the linear dependence of the UTDI laser pulse wavelength with time. With this wavelength/time characteristic, the spectral axis of the UTDI trace is readily converted to a high-resolution picosecond time sweep. This wavelength/time conversion was used to estimate the time history of the UTDI pulse from the directly measured pulse spectrum as shown at right in Fig. 2. Here, the rise time of the pulse has been estimated at ~25 ps, based on the 10%-90% intensity points.

A sample UTDI trace obtained from a polystyrene-on-aluminum sample is shown in Figure 3. A reference interferogram from a static surface without shock drive is shown in at top, while data from the same sample during with the laser drive applied are shown below. The vertical axis represents a 1-D cut through the center of the pump-beam spot, with a resolution of 1.5 μm/pixel. Time is represented on the horizontal, where the resolution in the measurement is 10 ps. In each case, the full-field interferogram is shown on the left, and "zoomed in" results that highlight the impact of laser drive at time t = 350-450 ps are shown on the right. The fringes in the reference data are essentially straight, while the results with laser drive reveal fringe curvature as a result of phase shift that is accumulated within the delay, Δt, between the probe laser pulses. Phase shifts in the UTDI data are analyzed to yield the ablator or piston velocity (U_p), the shock velocity (U_s), and the shocked index of refraction (n_s) in the material. UTDI measurements can then be performed over a range of laser drive conditions to vary shock drive pressure and extract U_s-U_p Hugoniot data according to the physical model which describes the canonical USI response that is presented next.

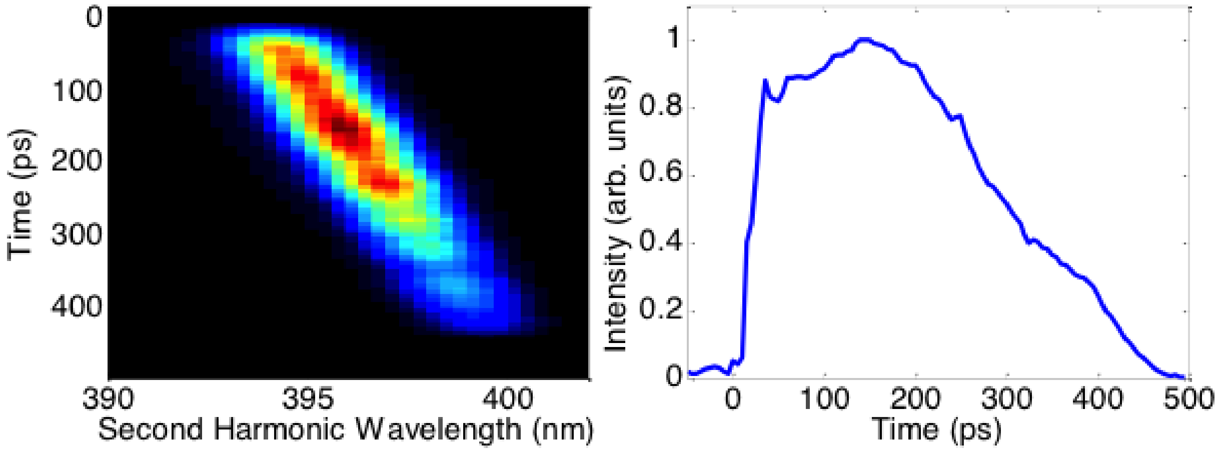

Figure 2 Characteristics of temporally chirped laser pulse for UTDI measurements. Second-harmonic FROG trace showing the time dependence of the laser wavelength that encodes time into the spectral domain (left). Extracted laser pulse shape with rapid ~25 ps rise.

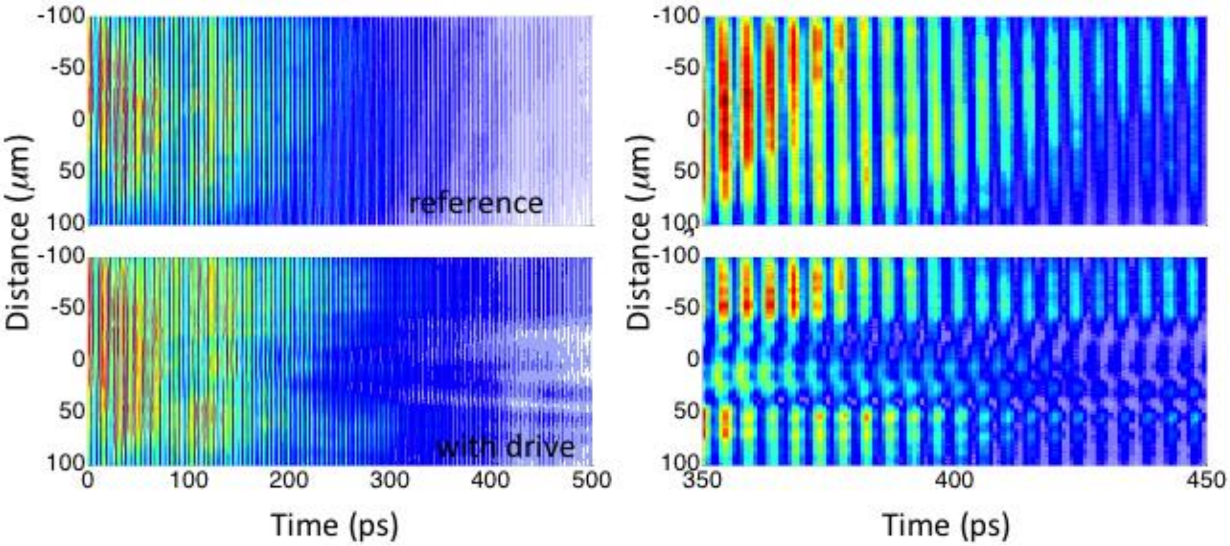

Figure 3 Interferogram generated when a probe pulse pair interacts with the UTDI sample. Reference data with no drive pulse applied are shown at top and interferograms with the drive pulse applied are shown at the bottom. Full field data are shown at left, while a region of interest in the vicinity of the laser drive is shown at right.

2.2 Physical Model and UTDI Working Principles

If we consider a steady-state shock entering an unreacted material, the shock wave traveling at speed $U_s > U_p$ creates a region of compressed material where the shocked index of refraction, n_s, exceeds the unshocked index of refraction, n_o, as in Fig. 4 below. Reflections of the probe pulse pair of Fig. 1 that arise from the aluminum ablator and the shock front are additionally considered in Fig. 4. As shown by Armstrong *et al.* [2], phase shifts in the complex-valued ablator and shock-front reflectivities accumulated during the ~10-ps delay between the probe pulse pair give UTDI its sensitivity to shock-wave parameters. The reader is referred to ref. [2] for a more detailed discussion, while a phenomenological summary of UTDI working principals is provided here. The canonical UTDI response is composed an ablator part and a contribution from the two first-order reflections from the shock front: a direct, Doppler-shifted reflection from the moving shock wave, and a contribution from what is effectively a scanning optical etalon formed by multiple reflections between the shock and ablator surfaces, as depicted in Fig. 4. The canonical UTDI response that results from these reflections is shown in Fig. 5. A constant offset, $\Delta\theta_m$, arises from ablator motion and the refractive index jump within the shocked region, whose thickness scales as $U_s - U_p$.

$$\frac{\Delta\theta_m}{\Delta t} = \frac{4\pi}{\lambda}\left(n_s U_p - \Delta n U_s\right) \tag{1}$$

In Eq. 1, λ is the probe-pulse wavelength, and Δn is the jump in refractive index across the shock front. The region between the shock front and the ablator additionally represents an optical etalon of time-varying thickness, whose complex-valued reflectivity varies periodically as the shocked region thickness passes through integer-multiples of the probe light's optical path. The reflectivity is then expected to have a phase contribution which varies periodically, with period τ, as

$$\tau\left(U_s - U_p\right) = \frac{\lambda}{2n_s} \quad . \tag{2}$$

This canonical response is then characterized in terms of an initial rise to the phase offset $\Delta\theta_{\mathrm{m}}$, and an oscillatory part with period, τ, and amplitude, δ, which can be extracted from a fit to the oscillatory portion of the measured phase-derivative response. Armstrong's detailed analysis [2] relates these measured phase shift parameters to shock wave properties.

$$U_s = \frac{\lambda}{4\pi n_0}\left[\frac{\Delta\theta_m}{\Delta t} + \frac{2\pi}{\tau}\right] \tag{3}$$

$$U_P = \frac{\lambda}{4\pi n_0}\left[\frac{\Delta\theta_m}{\Delta t} + \frac{2\pi}{\tau}\left(1 - \frac{n_0}{n_s}\right)\right] \tag{4}$$

$$n_s = n_0 + \frac{\tau\delta n_0}{2\pi\Delta t - \tau\delta} \tag{5}$$

Once U_s and U_{p} are determined, the shock pressure can be determined from the Rankine-Hugoniot jump conditions across a steady shock wave as

$$P = \rho_o U_s U_p \quad . \tag{6}$$

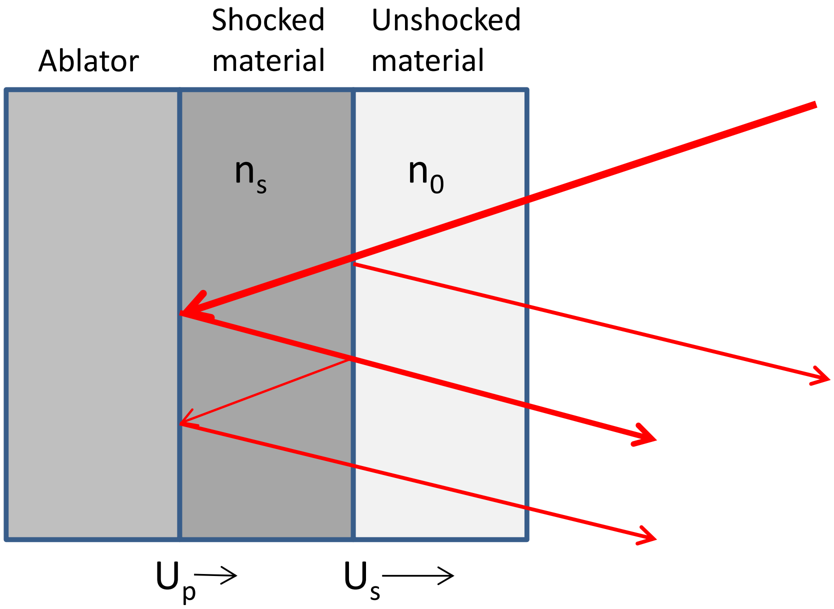

Figure 4 Physical model to describe reflections from the shock front and ablator surface. Only the first-order reflections from the shock front and ablator are considered in the analysis.

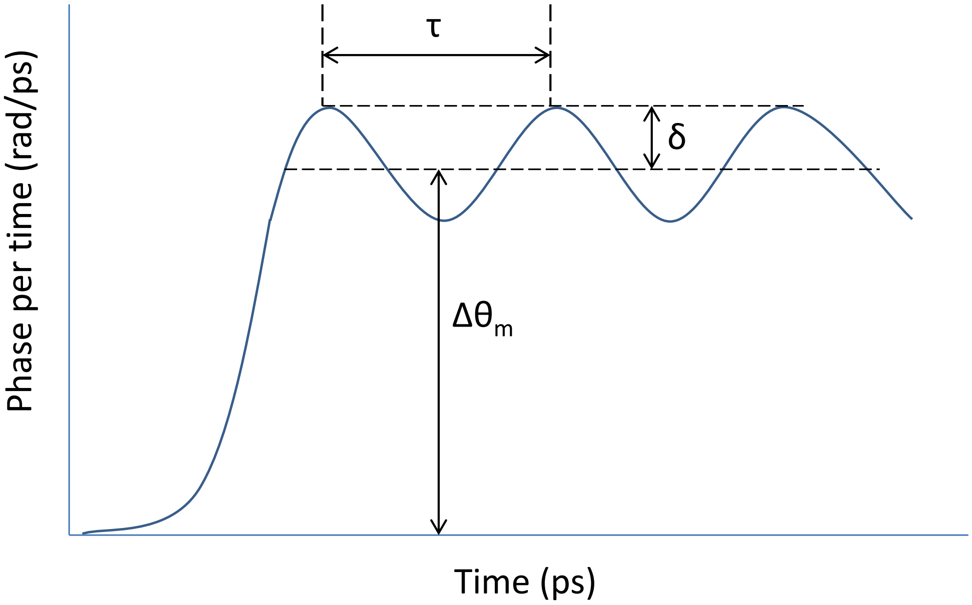

Figure 5 Canonical UTDI trace of phase accumulated per unit of time equal to the probe pair separation. The offset ($\Delta\theta_m$), amplitude (δ), and period (τ) are measured quantities used to determine U_s, U_p, and n_s.

2.3 Sandia UTDI Experiment

The experimental apparatus constructed at the Sandia Explosive Components Facility (ECF) is similar to that used in previous work [2], and with key elements as shown in Fig 1. A commercial Ti:Sapphire amplifier (KM Labs Wyvern) provides 4-mJ pulses of 42-fs duration at 1-kHz repetition rate. The amplifier output spectrum is centered near 790 nm, with a bandwidth of 25 nm (FWHM). A user-selectable portion of the ~170-ps regenerative amplifier output energy is extracted before compression and further stretched in an off-design external grating compressor, so that the blue edge of the spectrum leads the red. A fast time-domain rise is added to the pulse by clipping the dispersed spectrum within the compressor. Previous work [2-10] using an external stretcher, produced 10- to 20-ps rise shock waves in aluminum films. In the "overcompressed" pulse-shaper design used here, *lack of a true Fourier plane in our external compressor may result in a more gradual rise to the clipped spectrum and time-domain pulse.*

The bandwidth-clipped and stretched pulse is relayed to the sample in the arrangement shown in Fig. 1. The majority of the pulse energy is delivered to the pump (shock drive) beam directed onto the back side of the samples; 2-μm thick aluminum films deposited on a glass substrate were utilized either in bare condition or with an inert (polystyrene/sylgard) or explosive (HNAB) stacked onto the ablator. The pump beam is focused at a numerical aperture (NA) ~0.03 using a f = 150-mm convex lens. The pump then focuses through the glass substrate to a ~20-30-μm spot at the back surface of the aluminum ablator, where the momentum exchange from the formation of laser-induced plasma drives a shock wave into the film. A small fraction of the pulse energy is split via a Michelson-type interferometer, where a delay is introduced to form the collinear probe-pulse pair that is directed to the sample through a polarizing cube with circular polarization imparted by a quarter-wave plate. Nominal delay between the probe pulses is ~10-15 ps, as determined from the fringe spacing in the UTDI interferograms. The probe-pulse pair is weakly focused at normal incidence onto the sample through the combined effect of a 2× microscope objective of 0.07 NA and a f = 500-mm lens placed in the probe beam path. Introduction of the 500-mm lens permits proper imaging of the sample plane with a probe that is only weakly focused to ~100-μm, 3× larger than the pump-beam spot that is centered within the probe. Back-reflected probe-beam energy is collected through the microscope objective and rejected by the polarizer-waveplate pair onto the entrance slit of a 0.3-m grating spectrograph, where the pulses are spectrally dispersed and combined at the face of a CCD camera placed at the spectrometer focal plane.

The sample plane during a laser-drive experiment is depicted in Fig. 6 [2], where the deformation of the laser-driven ablator forms a "piston interface" behind an expanding shock front. For the conditions of a "typical" UTDI experiment described here, Armstrong [4] has shown that the radius of curvature of the shock front is large compared to the sample thickness, so that 1-D shock conditions exist locally within the film. We note that our experiment measures the piston speed, not the particle speed just behind shock front, but it has been shown in previous work [6] that, by assuming the particle speed is the same as the measured piston speed, the measured shockwave speed will correspond to the known Hugoniot to better than 2% accuracy [6, 11].

An in-house built MATLAB code has been constructed to extract the phase accumulation over the probe pair delay on a row-by-row basis within the shocked region by subtracting the complex-valued Fourier transforms of the shocked-region row data from reference regions taken outside of the shock-drive zone and in reference frames taken just before the laser-drive experiments, as shown previously in Fig. 3. Inverse transform of these results yields time-dependent phase derivatives of the type shown canonically in Fig. 5. The resulting phase fields are then fit to model Eqs. 3-5 to extract shock parameters.

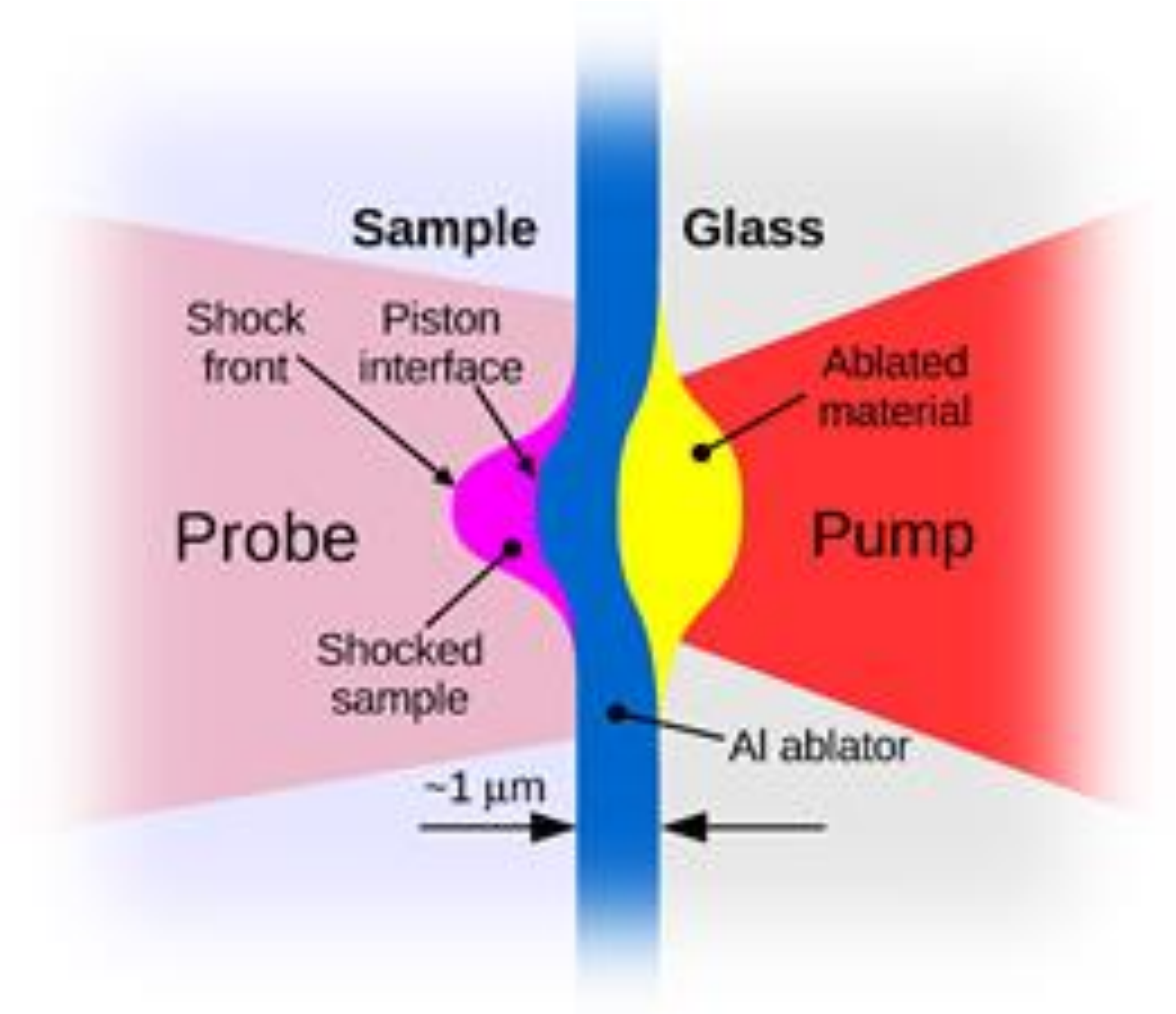

Figure 6 A schematic cross section of the experiment at the sample [2].

2.4 UTDI Results

2.4.1 Shock Breakout Measurements on Bare Aluminum Films

Measurements were initially performed on bare aluminum films to characterize the response of both the UTDI setup and the performance of the picosecond laser-drive for shock wave generation. Without a sample film, the velocity of the bare aluminum ablator, U_a, during shock breakout is related to the UTDI phase derivative by,

$$U_a = \frac{\lambda}{4\pi}\frac{\Delta\phi}{\Delta t} \quad . \tag{7}$$

Representative ablator velocity histories recorded in the ECF facilities in building 905 during shock breakout are shown in Fig. 7, where velocity traces for different drive pulse energies are shown. The velocity data are extracted from the region in the center of the drive pulse, where maximum surface displacement occurs. The data are consistent with very strong elastic precursors, as identified by Crowhurst *et al.* [11] in their UTDI investigation of the effect material thickness on direct laser drive. At drive pulse energies below ~500 μJ, the ablator response is characterized by an initial rise to a velocity plateau of U_a = 1-1.5 km/s, as a result of strong, but elastic deformation. The elastic wave is then followed by a second, more gradual rise to a higher speed resulting from a follow-on plastic deformation. As the drive pulse energy is increased, the duration of the velocity plateau following the elastic wave shortens and the maximum ablator velocity attained during the second, plastic wave increases to U_a ~ 4 km/s. Eventually, the drive pulse is sufficiently intense that the plastic wave overtakes the elastic precursor, resulting in single plastic deformation whose risetime is 20-30 ps. It is at this drive energy that a shock wave is present during ablator breakout.

The 500-μJ critical drive pulse energy identified here is significantly larger than observed in previous picosecond laser-drive experiments [2-12], where drive energies of only 50-100 μJ were sufficient to achieve plastic shock breakout in bare aluminum layers. At this time, we believe the reason for this is the stretcher design employed, which lacks a Fourier plane where the spectral elements are in focus. Clipping the laser bandwidth with out-of-focus spectral elements likely results in a more gradual initial rise in the drive pulse, so that more energy is needed to achieve steady shock conditions. This will become a factor in later investigations with inert and explosive material samples deposited on the aluminum layer.

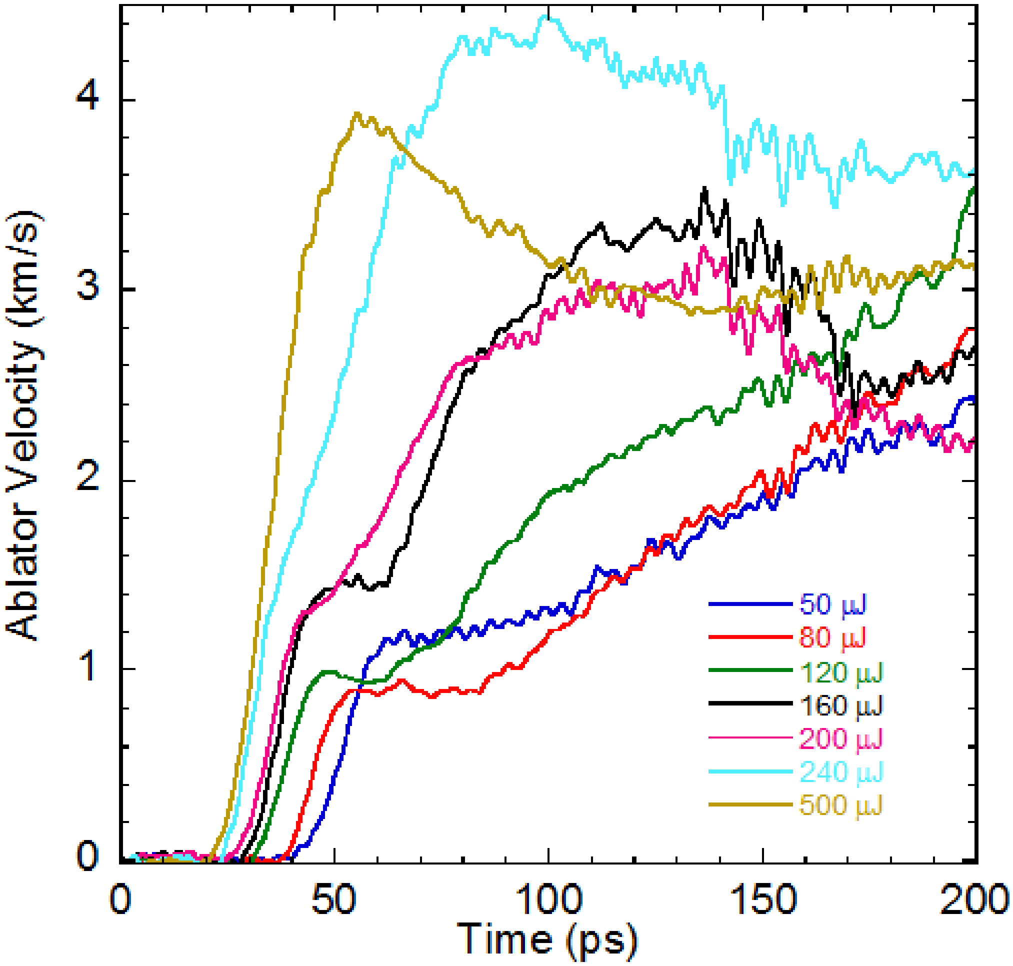

Figure 7 Aluminum ablator velocities with differing energies in the applied drive laser pulse. Data are from the Sandia ECF.

2.4.2 UTDI Measurements on Inert Films

UTDI experiments were conducted at the Sandia ECF with samples composed of inert polystyrene films and explosive PETN and HNAB films. The films were 3-5 μm thick and were all deposited on 1.5 μm aluminum ablators atop of microscope cover glass. Representative UTDI phase-derivative traces from polystyrene samples are shown for drive pulse energies from 120 to 250 μJ in Fig. 8. These phase histories are nominally similar to the expected canonical UTDI trace of Fig. 5, with an initial rise followed by a period of oscillating phase response. An in-house developed optimization routine was used to fit the oscillatory part of the traces within a user-defined time window, with the fits shown as the red curves in Fig. 8. In these experiments, the offset, $\Delta\theta_m/\Delta t$, was found to increase with time, as shown by the green curve, which represents a fit to a linearly varying offset. The mean value of $\Delta\theta_m/\Delta t$ from this fit was then used in Eqs. 3 and 4 to compute shock U_s and U_p. A similar linearly varying fit procedure was employed by Armstrong *et al.* in their UTDI measurements on shocked H_2O_2 [6], where unsteady piston speeds resulting from shock-induced chemistry resulted in a time-dependent phase offset. Here, we suspect that the observed time dependence in $\Delta\theta_m/\Delta t$ is a result of unsteady wave propagation in the experiments as a result of the above-mentioned slow rise in the picosecond shock drive pulse. We conducted additional experiments with drive energies in excess of 500 μJ in an effort to reach the steady shock behavior observed in the bare ablator results of Fig. 7. However, the quality of the UTDI traces at these high drive energies on the polystyrene samples was not sufficient for analysis.

Fitted (U_s, U_p) data from polystyrene data similar to that of Fig. 8 were used to construct a Hugoniot curve for unreacted polystyrene. The results are shown in Fig. 9, where data from the SNL ECF lab are plotted as open, blue circles and compared to historical data for “fully dense” polystyrene compiled by Marsh [13]. The UTDI measurements from SNL lie ~10-12 % above the historical polystyrene Hugoniot. As a check, UTDI measurements on similar polystyrene films were provided from Lawrence Livermore [14], with their results shown in Fig. 10. In Fig. 10a, representative UTDI phase histories are plotted, where the phase offset in the oscillatory portion of the trace appears approximately constant, in contrast to the results from Sandia shown in Fig. 8, suggesting a more steady shock drive in the Livermore experiments. Shock-Hugoniot data extracted from traces like those in Fig. 10a are shown in Fig. 10b, where three UTDI results are plotted as open, colored circles against the same historical data from Marsh shown in Fig. 9. In this case, the Livermore data reveal that the UTDI technique is capable of faithfully reproducing accepted shock Hugoniot data for a well-understood inert material.

Departure of the Sandia UTDI data from historical gas-gun data and Livermore UTDI results is likely a result of unsteady wave propagation in the polystyrene film, such that the speed of the post-shock material and the measured piston velocity do not equilibrate during the experiment. The consistently upward slope in the UTDI phase derivative data of Fig. 8 suggest that the wave speed is consistently increasing throughout the measurement.

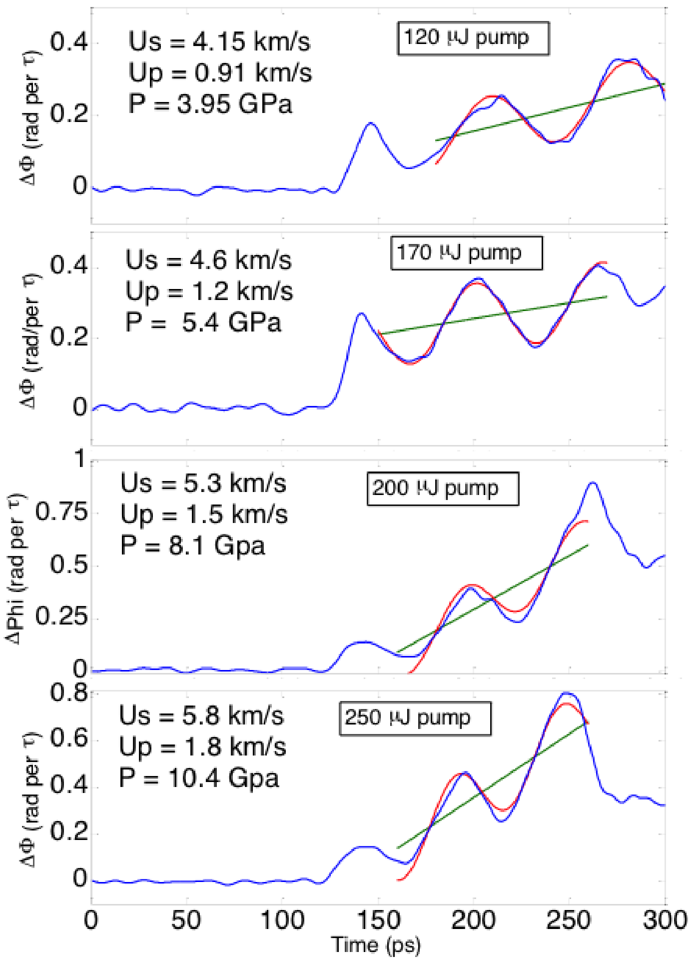

Figure 8 UTDI phase derivative traces obtained for polystyrene-on-aluminum samples at the Sandia ECF.

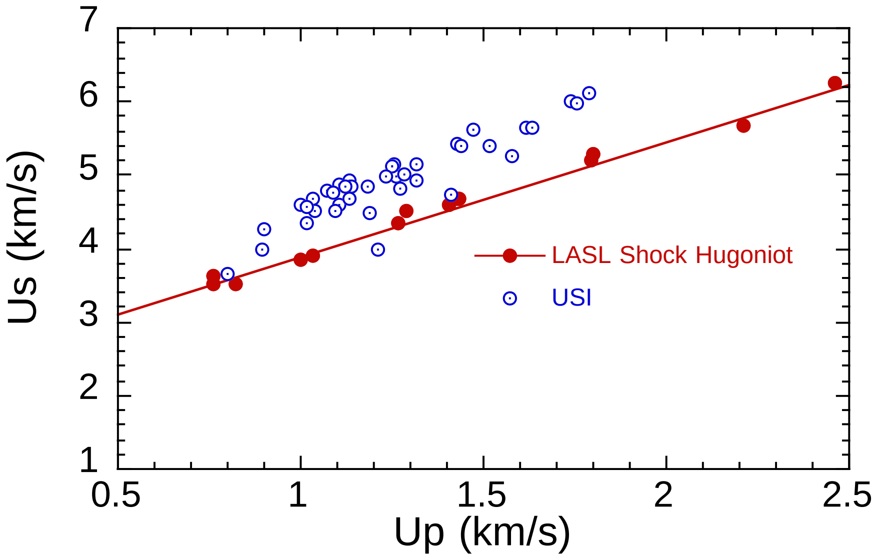

Figure 9 Polystyrene shock Hugoniot data extracted from UTDI phase derivative traces obtained at the Sandia ECF.

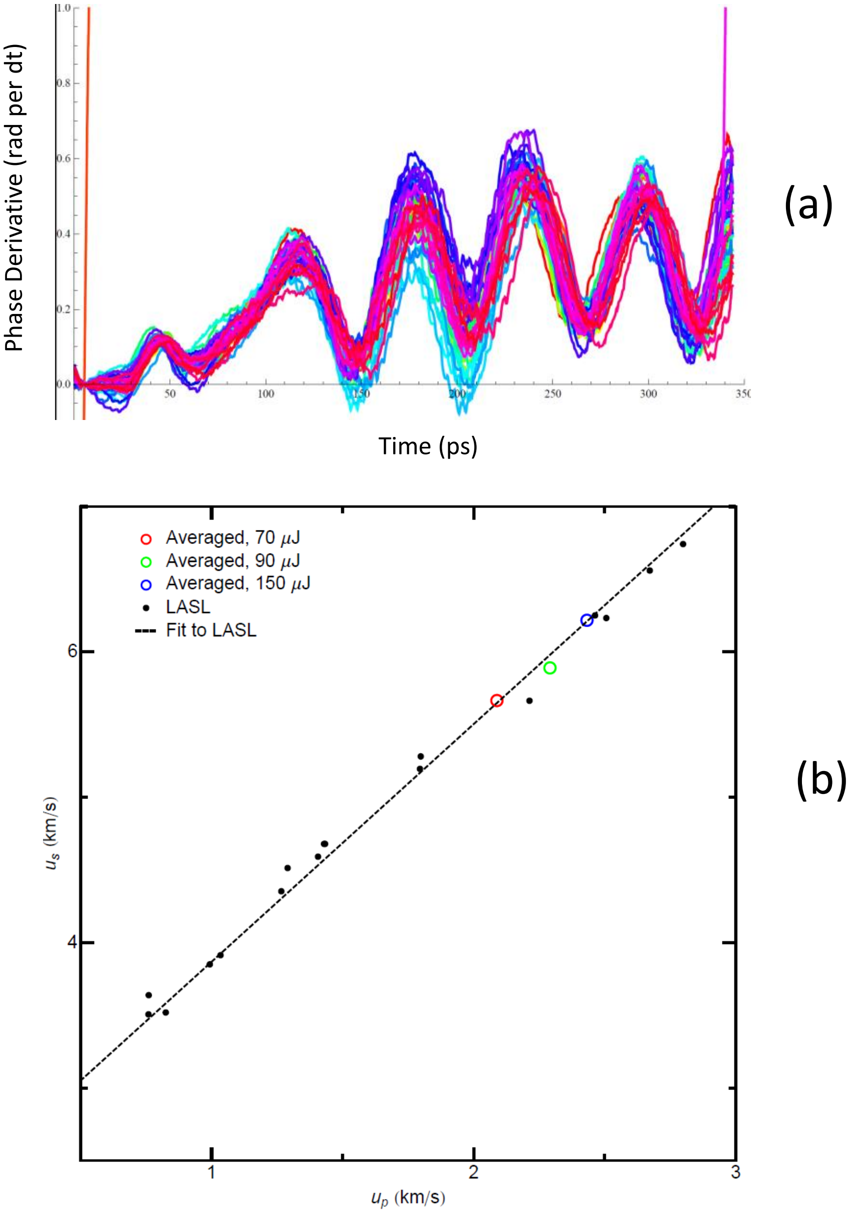

Figure 10 UTDI data recorded on polystyrene samples at Lawrence Livermore. Sample single-shot phase derivative histories are shown in (a). Extracted U_s/U_p shock Hugoniot data are shown in (b).

2.4.3 UTDI Measurements on HNAB films

Hexanitroazobenzene (HNAB) is an energetic material with properties that make it a model system to study the effects of microstructure on initiation. HNAB can be vapor-deposited as a fully dense amorphous film. If kept at room temperature, it crystallizes into a dense film (99.4% TMD) with nanometer-scale pores [15]. In the amorphous state, it shares some properties with liquid explosives: it has an isotropic molecular network (no long range order) and lacks micron-scale pores that can serve to nucleate shock-induced chemical initiation. Unlike liquid explosives, solid explosives like HNAB form much stronger intermolecular bonds. Detonation studies may be conducted on crystalline and amorphous HNAB to elucidate how pores and molecular ordering affect the shock initiation threshold. The material we probed was comprised of the HNAB II polymorph whose indices of refraction, required for UTDI analysis, vary with crystal orientation from 1.5 to 1.8 [16]. The films are randomly-oriented polycrystals so the average refractive index should lie somewhere between those two values. Here we used 1.8 for the index of refraction. UTDI experiments were performed on HNAB films at both the Sandia ECF and at Lawrence Livermore. All HNAB films were fabricated at Sandia.

UTDI phase-derivative traces acquired at Sandia are shown in Fig. 11, with fits to the oscillatory portion of the trace displayed in red and the linear fit to the phase offset shown in green. These Sandia experiments were conducted with constant energy in the drive laser pulse near 500 μJ, and the phase offset during the fitted portions oscillatory phase of these traces appears to be improved over the polystyrene results shown in Fig. 8. The extracted shock Hugoniot parameters display U_s = 5.1 − 5.5 km/s with U_p = 0.92 – 1.2 km/s, with an average value of (U_s, U_p) = (5.2, 1.1) km/s. A representative HNAB UTDI history obtained a Lawrence Livermore is shown in Fig. 12. The fitted oscillatory part and phase offset reveal that conditions during the Livermore experiments were not perfectly steady.

UTDI-determined shock Hugoniot data for HNAB are presented in Fig. 13. The results were obtained using an unshocked index of refraction of n_o = 1.8, as index measurements for the as-deposited films were not available. The density of HNAB was taken to be 1.750 g/cm^3 as measured from flotation in an aqueous barium perchlorate solution [17]. The data seem to lie upon a line except for a single outlier at the highest piston velocity. The plot of phase data for this point was not as well-behaved as the others, so it is likely that a steady shock was not present, and thus, the physical model used to derive Eqs. 3-5 was not satisfied. This single outlier was eliminated, we then ordered all the remaining data points by piston velocity, binned them in groups of 5, and averaged the U_s and U_p values by bin to create a Hugoniot plot with less scatter, as shown in Fig. 14, with tabular data provided in Table 1. Both data from Livermore and the four-shot averaged result from Sandia are included on the plot. A linear fit to the Livermore data results in an HNAB shock Hugoniot of U_s = 2.70 + 1.77 U_p. The result from Sandia lies 10% above this Hugoniot curve, similar to the polystyrene results presented above, although the reason for the discrepancy here could very well result from changes to the morphology of the HNAB films with time, which could result in changes to their shock response, it is likely that the form of the shock drive pulse plays a role in the discrepancy.

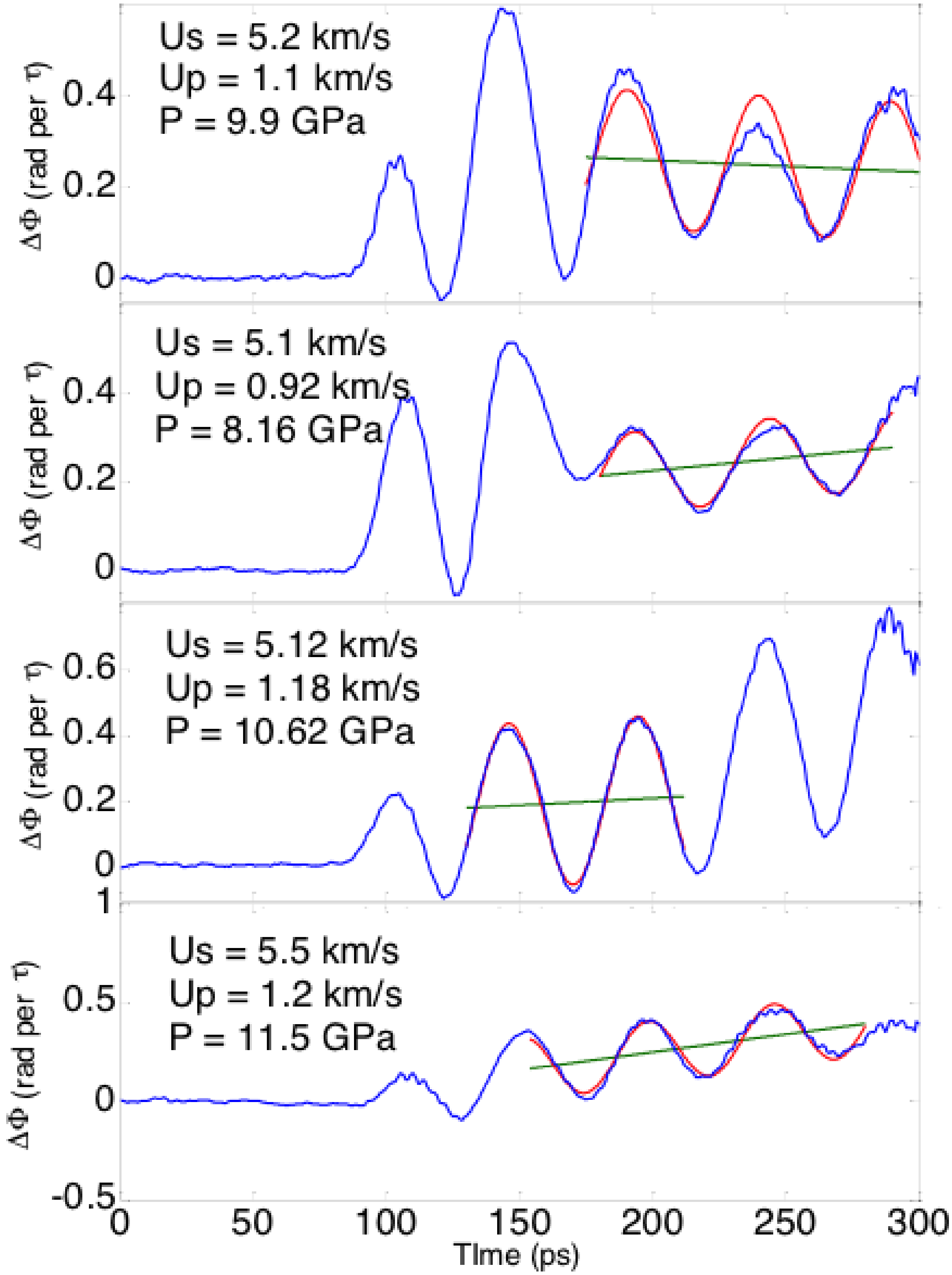

Figure 11 UTDI phase derivative traces obtained for HNAB-on-aluminum samples at the Sandia ECF.

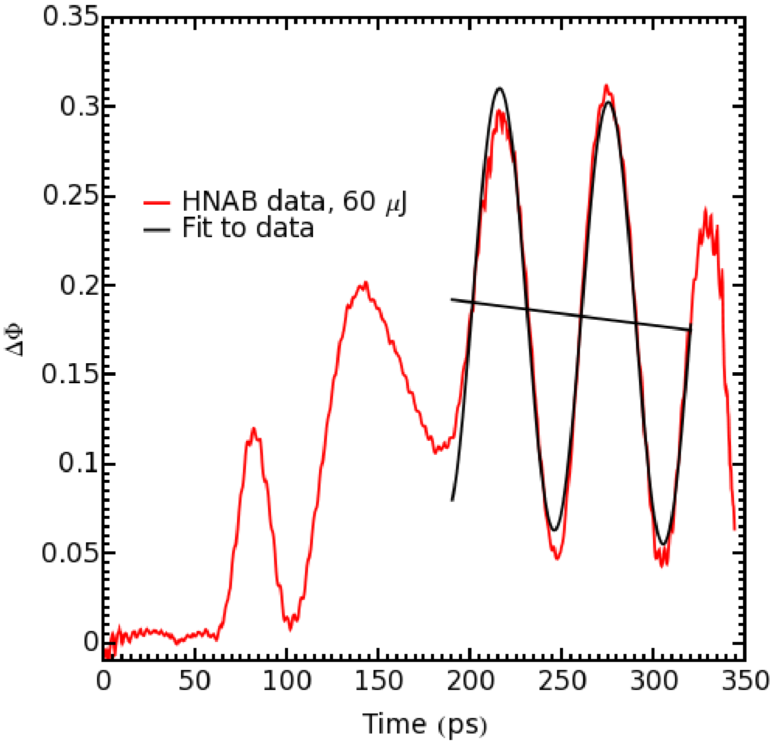

Figure 12 Phase data for HNAB and region used for fitting to the model. Data are from Lawrence Livermore.

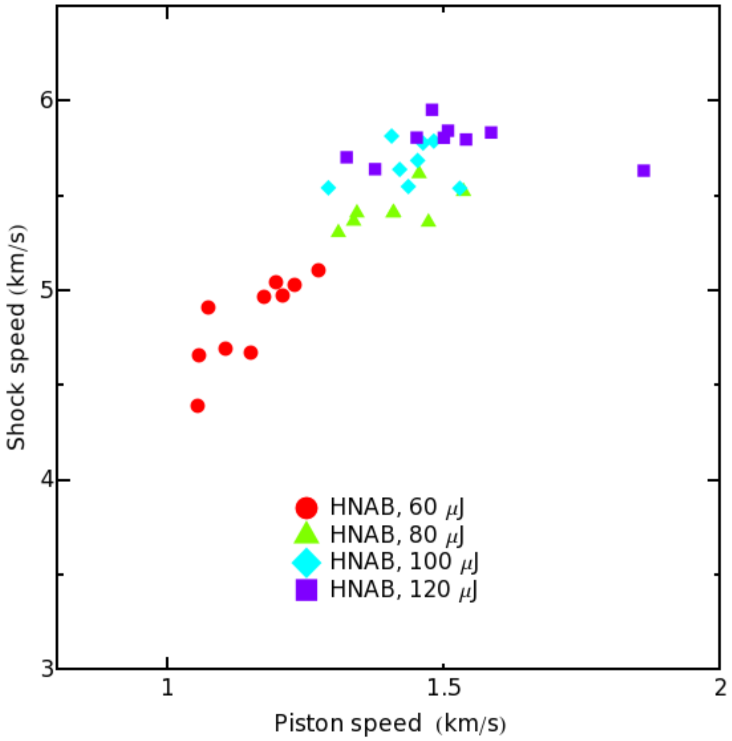

Figure 13 HNAB Hugoniot for all shots, ordered by pump energy. Data are from Lawrence Livermore.

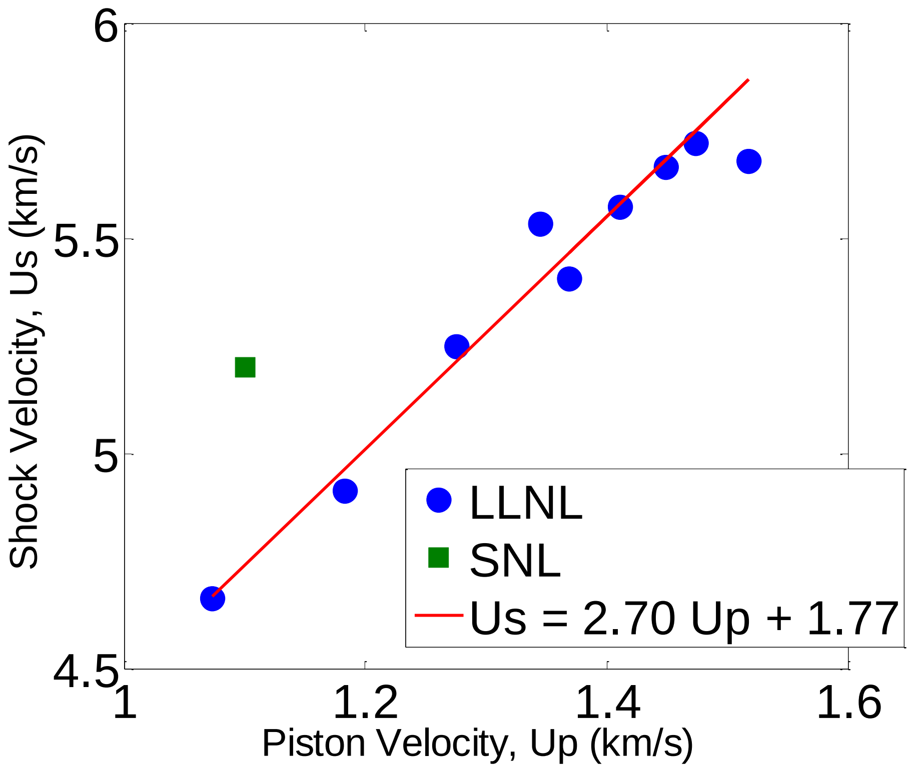

Figure 14 HNAB Hugoniot from Lawrence Livermore assuming n_o = 1.8.

Table 1 HNAB Hugoniot data assuming n_o = 1.8.

U_P (km/s)	U_S (km/s)
1.073	4.663
1.183	4.913
1.276	5.248
1.345	5.534
1.411	5.573
1.449	5.665
1.474	5.721
1.518	5.679
1.369	5.407

3. STIMULATED RAMAN SCATTERING AS A TEMPERATURE PROBE

3.1 Introduction

Temperature is a quantity that impacts kinetics of physical and chemical processes, and yet it is often not measured in solids due to its difficulty. In order to advance development of detailed models for shock induced initiation with proper treatment of molecular-level reactions, temperature must be extracted and provided as support data. For the fundamental description of ultrafast shock responses in energetic materials, it is important to have means for access to temperature at short time scales (~ps) over small volumes (~μm^3) as ignition mechanisms may depend on ultrafast energy transfers and complex microstructures within the material.

A number of techniques have been used to measure temperature in the gas phase using Raman techniques such as spontaneous Raman scattering and coherent anti-Stokes Raman scattering [18]. But some of these techniques have limitations for temperature measurement in small-volume solids. For example, in spontaneous Raman spectroscopy, the scattering rate is so low that long acquisition time are required and background signals could obscure spectral features. CARS approaches require use of models which are tractable for gases, but would be difficult for complex solids.

Femtosecond stimulated Raman scattering offers a method of measuring temperature in solids [19, 20]. This technique is analogous to the spontaneous Raman method of using anti-Stokes to Stokes signal ratio to extract vibrational temperature. The advantage of femtosecond SRS is that the scattering rate is orders of magnitude larger than that for spontaneous Raman scattering. This offers an opportunity to measure temperature in small-volume solids with short integration times. As an added benefit, the phase-matched output in the former allows for rejection of background fluorescence for higher signal-to-noise ratio. In contrast to CARS, the SRS measurement relies simply on the anti-Stokes to Stokes signal ratio and is independent of material parameters. The analysis therefore is simplified and involves a fitting routine to the data set as opposed to model development.

SRS occurs when pump and probe pulses overlap in time and space within a medium characterized by $\chi^{(3)}$. SRS is generally described as an exponential amplification of the probe pulse in the presence of the pump pulse in a material with differential cross section for Raman scattering as indicated in the expression below.

$$I_{SRS}(L) = I_{probe}(0)\exp(GL) \text{ , where } G \propto \left(\frac{\partial^2 \sigma}{\partial\omega\partial\Omega}\right) I_{pump}. \tag{8}$$

The differential cross section can be written in terms of the phonon thermal population and when accounted for in the SRS signal intensity for the anti-Stokes (loss) and Stokes (gain) components, the signal expressions can be written respectively as [19]:

$$I(\omega_{AS}, L) = I(\omega_{AS}, 0)\exp\{-C_{AS}[1-\exp(\hbar(\omega_p - \omega_{AS})/kT)]\} \tag{9}$$

$$I(\omega_S, L) = I(\omega_S, 0)\exp\{C_S[1-\exp(-\hbar(\omega_p-\omega_S)/kT)]\} \tag{10}$$

The constants C_{AS} and C_S are proportional to the pump intensity, differential cross section, and length of the medium and are independent of temperature. The ratio between these components retains temperature dependence and can be used for extracting temperature after the measurement of the SRS loss and gain intensities is performed.

3.2 Experiment

The femtosecond SRS experiment involves overlapping in time and space a narrowband pump pulse and a broadband probe pulse in a sample of interest to drive the SRS nonlinearity. For this experiment, these pulses were derived from a 1-kHz Ti:sapphire multi-pass amplifier with 2 mJ per pulse centered near 770 nm. This beam was split into the pump and probe beams. The pump pulses were filtered with a 775-nm interference bandpass filter with 25 cm^{-1} FWHM bandwidth. The probe pulses were not filtered and maintained their ~422 cm^{-1} bandwidth and ~60 fs pulse duration. See Figure 15 for general characteristics of the pump and probe pulses. (The original configuration of this pump-probe setup included white light generation in the probe beam to enable wider coverage of Raman modes. This is an effective probe, but care must be taken to control dispersion of the pulse as well as the spatial profile of the different wavelengths.)

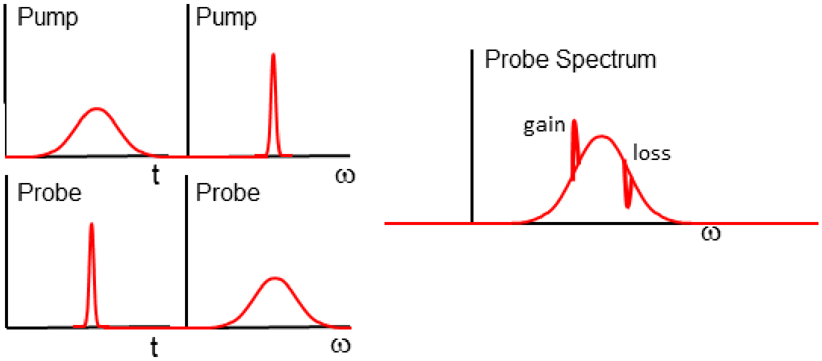

Figure 15 Pump and Probe pulses for SRS.

The pump and probe pulses were attenuated using variable neutral density filters to 5 μJ and 0.1 μJ respectively. As shown in Figure 16, the two attenuated beams were focused and overlapped in the sample using an f=200mm lens for the pump and f=150mm for the probe. A translation stage was used to time delay the pump pulses to coincide with the probe pulses at the sample. Halfwave plates were used in both beams to control the polarization. After the sample, the probe beam was re-collimated and then focused into a spectrometer, and its spectrum was detected on a CCD. A photo of the experimental setup is shown in Figure 17. For temperature dependent measurements, a liquid nitrogen cryostat and a resistive heater were used to reach the temperature range between 77K and 500K.

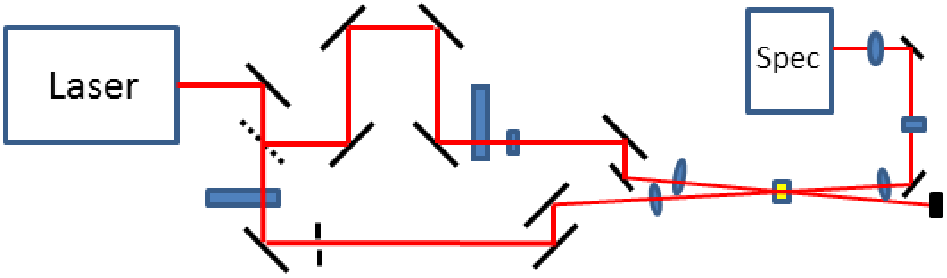

Figure 16 Experimental setup for SRS.

The samples used in the experiments were crystalline calcite and quartz. For calcite (100), the sample was 1 mm in thickness and the observed Raman modes were located at 155 cm^{-1} and 282 cm^{-1}. The quartz sample was 1.5 mm in thickness and the Raman modes were measured at 147 cm^{-1} and 207 cm^{-1} [21].

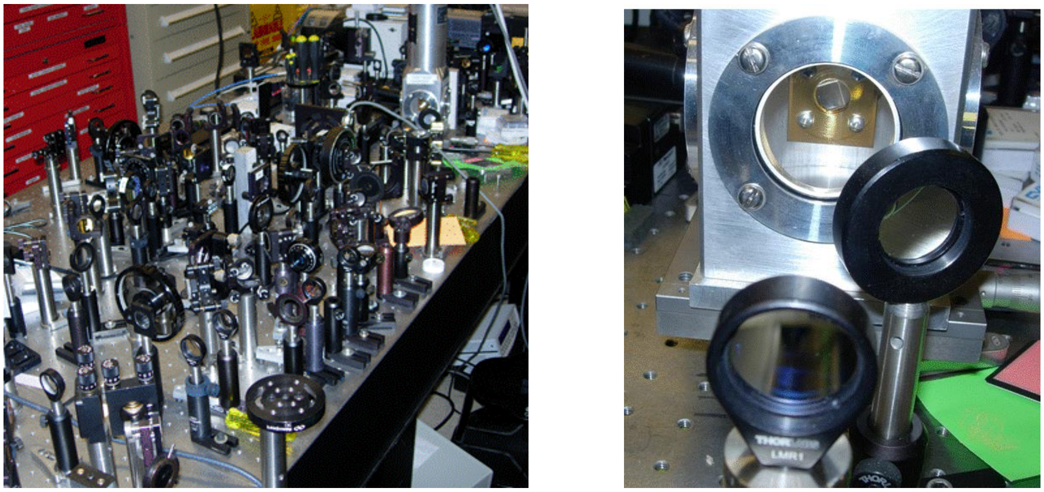

Figure 17 a) Photo of experimental setup for SRS. b) Photo of quartz sample in cryostat.

The acquisition sequence consisted of recording the SRS probe on the CCD with adequate SNR with the pump on and pump off. The SRS loss and gain spectra were obtained by subtracting the pump-off spectrum from the pump-on spectrum and normalizing with respect to the pump-off spectrum.

3.3 Measurement Results

Figure 18 shows the SRS spectrum for crystalline quartz measured at 140 K. The pump-on and pump-off spectra were subtracted and then normalized to generate this plot. With the narrowband pump centered near 775 nm, the 147 cm^{-1} Raman mode appears at 766 nm and 784 nm as a negative anti-Stokes signal and positive Stokes signal respectively. The 207 cm^{-1} Raman mode shows up near 763 nm and 787 nm. The signal-to-noise ratio was adequate to extract loss and gain signal intensities. For this particular plot, 500 pulses were integrated on the CCD.

Although the relevant main features of the anti-Stokes loss signal and Stokes gain signal are visible, the Raman spectrum is dominated by a background signal that originates from nonlinearities that arise when the pump and probe pulses overlap in the sample. Trends observed in the background signal indicate that it originates mostly from cross-phase modulation. This background must be removed to obtain temperature information from the SRS signals.

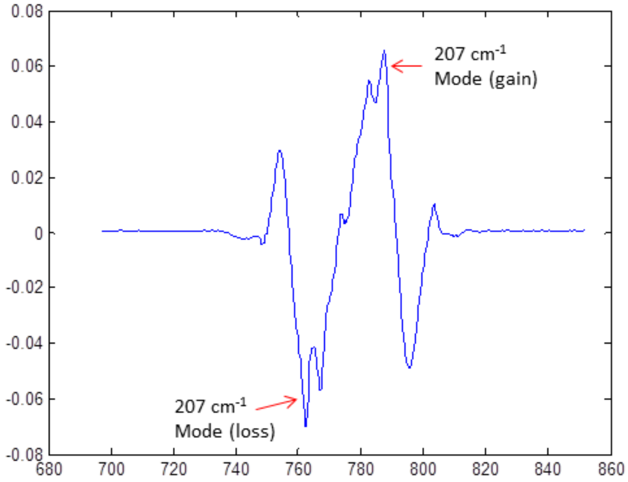

Figure 18 Raw SRS spectrum for quartz at 140 K.

In order to extract out the loss and gain signals from the raw SRS spectrum, a fitting and subtraction routine was written. Shown on Figure 19 as an example are the spectral sections of the raw SRS spectrum corresponding to the anti-Stokes and Stokes signals. The blue dots represent the acquired data and the red curve depicts a polynomial fit to the background nonlinear signal. As the cross-phase modulation component is relatively well behaved, this subtraction routine removes the background in a manageable way. It should be noted that during the acquisition process, when the laser is stable, these background features are reproducible and stable. In spite of this, the greatest source of error in the SRS analysis comes from this subtraction process.

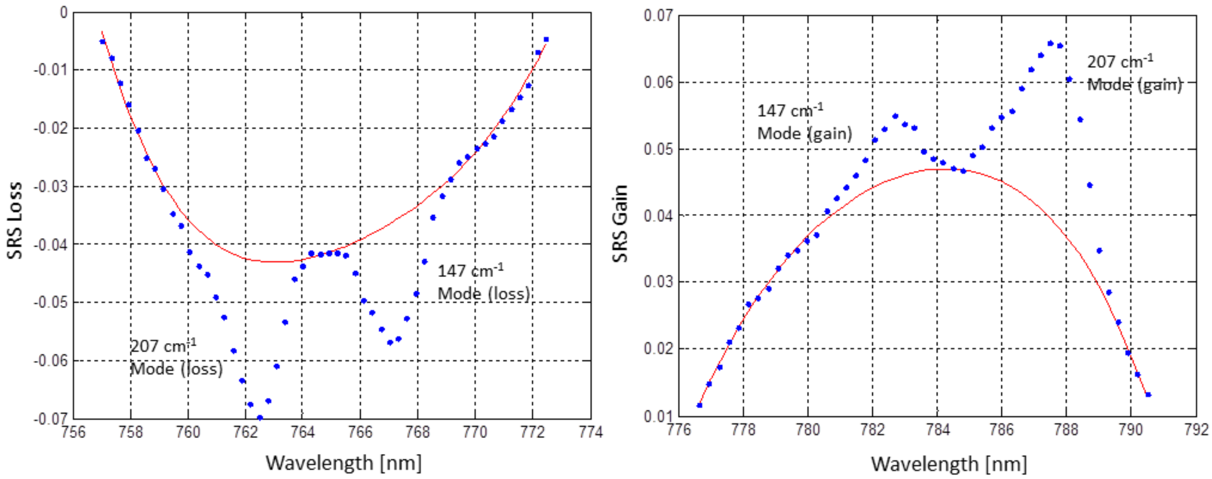

Figure 19 Raw a) anti-Stokes and b) Stokes SRS spectrum for quartz at 140 K. Line in red is the fitting curve used to remove background signal arising from nonlinear effect.

When the baseline correction is made, the loss and gain spectra appear as those in Figure 20. Here, the data from Figure 19 are directly processed, and the paired 147 cm^{-1} and 207 cm^{-1} Raman modes are clearly observed as negative anti-Stokes signals and positive Stokes signals.

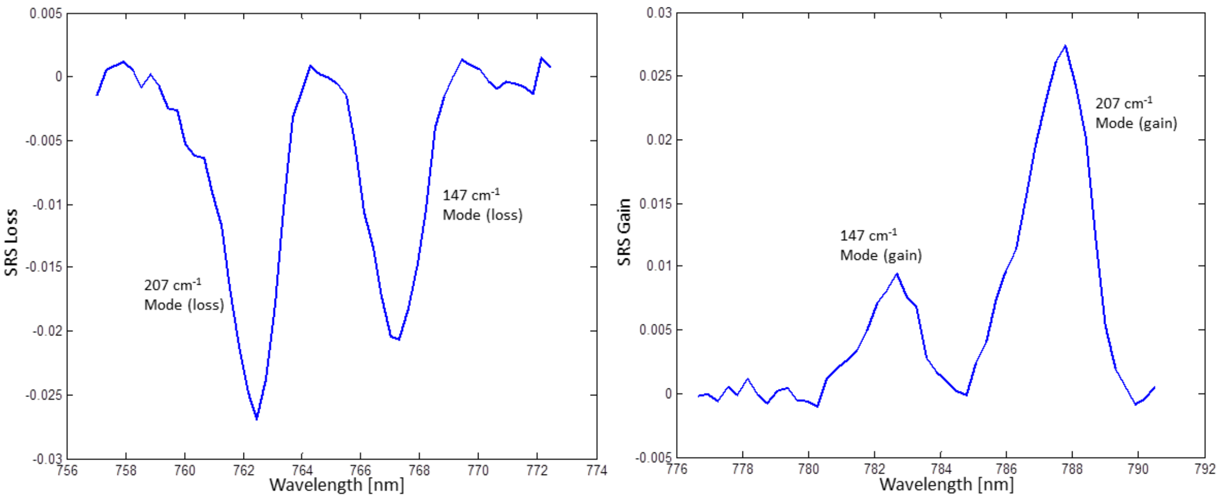

Figure 20 Background subtracted a) anti-Stokes and b) Stokes SRS spectrum for quartz at 140 K. Background originating from pulse induced nonlinearities.

3.4 Discussion

For demonstration of the thermometric capabilities of the femtosecond SRS method, SRS data sets were measured and analyzed over the temperature range of 77K to 500K. Plotted in Figure 21 is a set of curves representing the SRS ratio as a function of temperature. These curved were generated by evaluating the anti-Stokes to Stokes signal ratio from the expressions given for loss and gain above. The five curves correspond to five different gain values assigned to the SRS interaction. The lowest curve has the highest gain, and it shows that over the temperature range of 100K to 500K, higher temperature sensitivity is achieved at higher gain levels. These numerical results will be compared to measured data to verify the predictive matching of temperature trends.

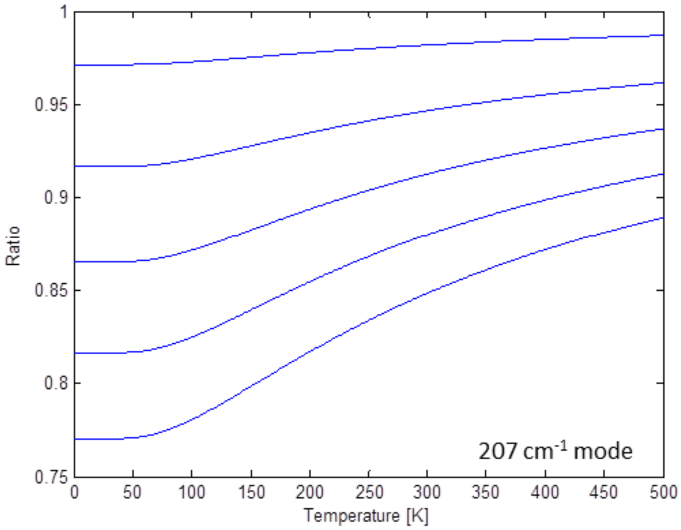

Figure 21 Plot of SRS ratio as a function of temperature as predicted by theory for the 207 cm-1 mode of quartz. The different curves represent different levels of Raman gain generated in the sample

Figure 22 shows a plot of the measured 207-cm^{-1} anti-Stokes signal level and the corresponding numerical result as a function of temperature. Apart from the outliers at 77 K and 350 K, the measured data points generally follow the expected trend. The error values arise mostly from the uncertainty in the fitting routine as mentioned above.

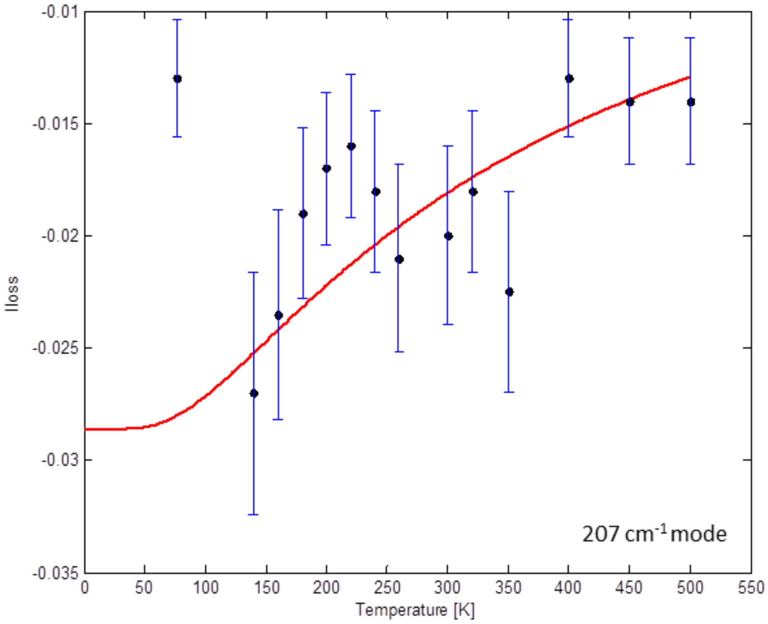

Figure 22 Plot of $I_{Anti-Stokes}$ as a function of temperature for the 207 cm^{-1} mode of quartz. The red line is the numerical result for $I_{Anti-Stokes}$.

Similar results for the Stokes signal for the 207 cm^{-1} mode are plotted in Figure 23. Again, there is a clear matching of the temperature trend between the data and numerical results. In the numerical analysis, the only parameter that is adjusted is the gain coefficient represented by C_{AS} and C_S in the above equations for I_{AS} and I_S.

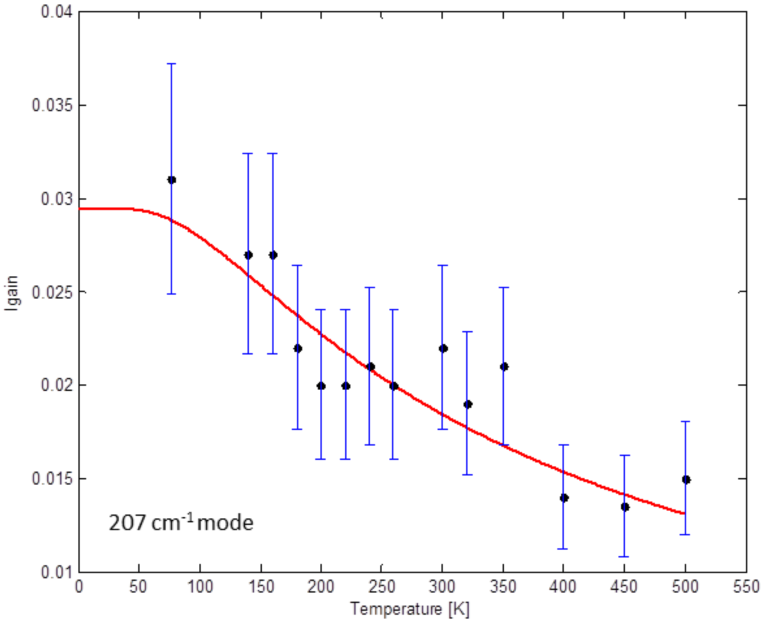

Figure 23 Plot of I_{Stokes} as a function of temperature for the 207 cm^{-1} mode of quartz. The red line is the numerical result for I_{Stokes}.

Combining the results for anti-Stokes and Stokes signal levels, the SRS ratio as a function of temperature for the 207 cm^{-1} mode is presented in Figure 24. Except for the outlier at 77K, the data points well match the expected values. That is, the trend of the SRS-ratio data is captured by the numerical results. But the error in the measurement as well as the strength of the gain induced by the pump pulses do not provide a very precise measure of the temperature in this particular acquisition. Given that the SRS signal levels and the ratio follow the numerical results well, femtosecond SRS provides thermometric capability for interrogation of solids. For precision in temperature measurements, significant care must be taken during the acquisition procedure to optimize the SRS signal level for both the anti-Stokes and Stokes components.

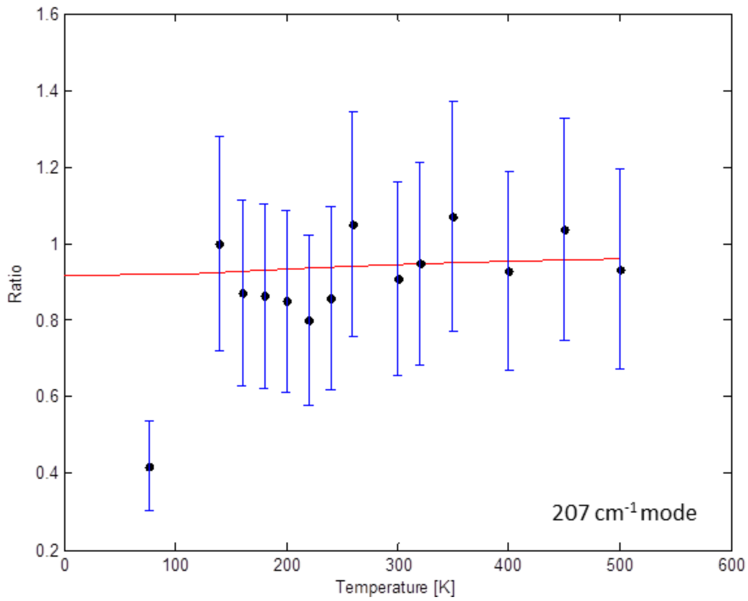

Figure 24 Plot of SRS ratio as a function of temperature for the 207 cm^{-1} mode of quartz. The red line is the numerical result for I$_{\text{Stokes}}$.

The following are some considerations that will need to be addressed in order to increase the precision on the SRS measurement and analysis.

- Increasing the gain of SRS increases the temperature sensitivity of the SRS ratio curve. This gain increase can be achieved with increased pump pulse energies. But there is a limit to this as increased pump energies induce significant background nonlinear signals which distort the SRS spectrum. When the pump energy is increased to high levels, white light is generated within the sample making the SRS method intractable.
- Pump induced nonlinearities such as cross phase modulation need to be minimized by controlling the pump energy, sample thickness, and timing between the pump and probe pulses. The modulation observed in the SRS spectrum showed dependence on peak intensities and time delays. When the source laser is stable, these modulations are stable. For full analysis of the background contribution to the SRS spectrum, a full treatment of the field propagation within the material will have to be carried out.
- Spatial, spectral, and temporal characteristics of the pump and probe pulses need to be well examined. For an ideal SRS experiment, the spatial mode of the beams should be well characterized so that intensity values could be determined precisely over the entire bandwidth. The spectral and temporal properties of the probe pulse should be such that the arrival time of the different wavelengths is within tolerance of the measurement. During the experiment, care must be taken to ascertain that the anti-Stokes and Stokes signals are optimized simultaneously and that the peak signal levels are occurring at the same delay.
- Data acquisition needs to be set up so that the pump-on and pump-off spectra can be captured quickly so that impact of laser jitter could be minimized.
- A balance must be struck on sample thickness as higher thickness will generate more SRS signal as well as the background nonlinearity. For studies on thin

films, unless a material has unusually high optical response for SRS, SNR based on few hundred shots with ~micro Joules of pump pulse energy on a less than 100 μm sample would be difficult because of the achievable signal levels.
- SRS enhancement may be achieved through electronic enhancement by operating the experiment our in the shorter wavelength region. The pump could be generated using second harmonic and white light near the pump wavelength could be used for the probe. The drawback to this approach is the potential for increased noise in the white light.

The original plan for SRS in this project was to use SRS thermometry to measure temperature in thin films of energetic materials. We explored this option, but there were challenges as follows.

- For samples such as PETN, the surface and volume quality of the sample made intensity delivery too difficult. Due to the surface and volume roughness, the pump and probe pulses diffusely scattered making the measurement unmanageable.
- For samples such as HNAB and HNS, the SRS response was too weak on samples that were 10s of microns in thickness. In addition, the nonlinear response from the substrate dominated the probe signal.
- Sample burning was an issue on all film samples when the pump energy was increased to improve SRS response.
- In order to increase the interaction length, pressed pellets of PETN, HNAB, and HNS were examined. But these samples, as with the films, did not allow for clean transmission of the probe beam. There was cleaner transmission in HNS, but the SRS response was too weak.
- As with the quartz and calcite samples, the nonlinear signals were generated when the pump and probe pulses overlapped in the sample.

Based on this study, it does not appear that SRS could be used directly on dynamically driven energetic materials that are very thin and require single-shot acquisition. But if the laser or mechanical shock drive could be extended so that the sample thickness could be increased, there may be opportunity to take advantage of femtosecond SRS.

3.5 Broadband SRS Using OPA + SHG and other considerations

In order to improve upon the pump-probe SRS technique, a setup using the second harmonic of an optical parametric amplifier (OPA) for the probe pulses was built. This allowed for broader spectral coverage, improved amplitude and timing control of the anti-Stokes and Stokes probe pulses, and use of reference spectra during acquisition. The schematic of the setup is in Figure 25.

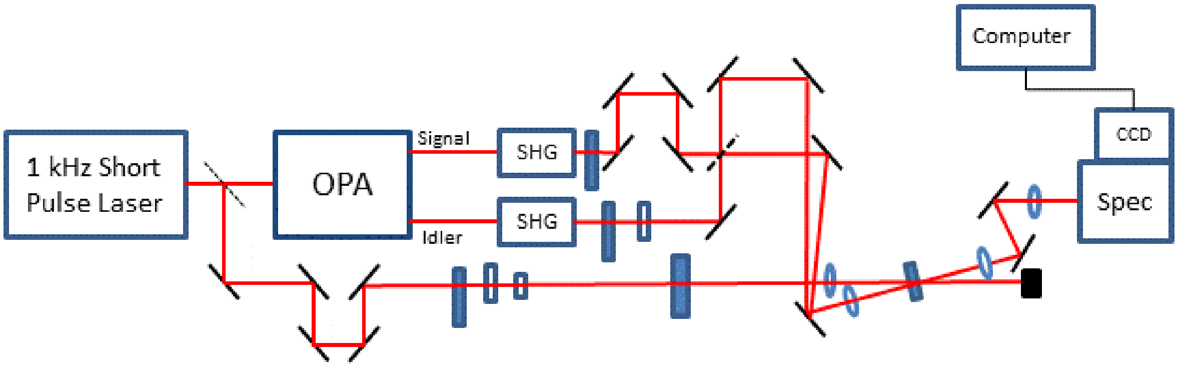

Figure 25 Experimental setup for broadband SRS.

The basic concept of the SRS experiment is the same, but now, the probe is composed of two separate pulses with one of them spectrally aligned for the anti-Stokes probe and the other for the Stokes probe. These pulses are generated by sending 1-mJ, 770-nm pulses into the OPA for IR signal and idler outputs (~10s of micro Joules). These OPA pulses are then frequency doubled in BBO nonlinear crystals to produce the SRS probe pulses. In order to generate reference pulses which are used to normalize the probe spectrum and to remove effects from variations in optical and detector responses, each of the probe pulse is split and spatially and temporally separated. These four probe pulses are then combined with the spectrally narrowed pump pulse at the sample as in the earlier setup. The signal probe pulses and reference probe pulses are collected into the spectrometer and detected on two different regions of the CCD. A shutter is used on the pump beam to capture the probe pulses with and without the pump.

For initial testing purposes, liquid benzene was used as the sample. Figure 26 shows the anti-Stokes loss and Stokes gain of the 990-cm^{-1} mode. There is a clearly defined signal for temperature analysis. There is also an improvement in the SNR considering that only 10 shots were taken for these plots. It should be noted that there is a broad feature at the base of the signals which would contribute to error in the analysis.

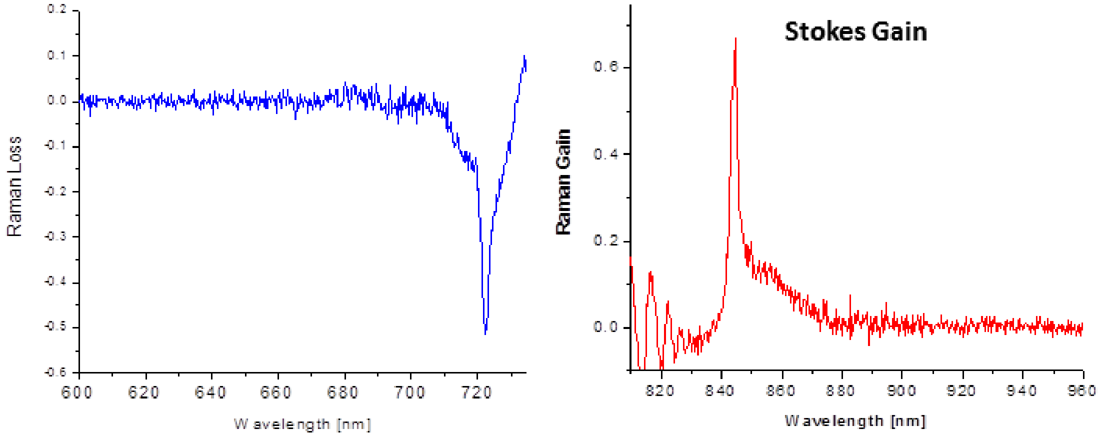

Figure 26 a) Anti-Stokes and b) Stokes SRS spectra from liquid benzene (990 cm^{-1} mode) using broadband SRS.

Results for a 3-mm calcite crystal are given in Figure 27. For these measurements, the pump energy was set to 13 μJ and the probe at 0.2 μJ. Ten shots per spectrum were acquired. The SNR was adequately high for temperature analysis (SNR for Stokes signal was > 20.). Although there continued to be a background shoulder in the anti-Stokes spectrum, the Stokes peak looked strong and showed only minor effects from the background nonlinear response. The contributing factors to this improved SNR were the i) spectral separation of the main part of the pump and the probe pulses, ii) spectral normalization with the use of reference spectrum, and iii) increased thickness of the sample (although this sample was only 2-3 time thicker than the quartz sample used above).

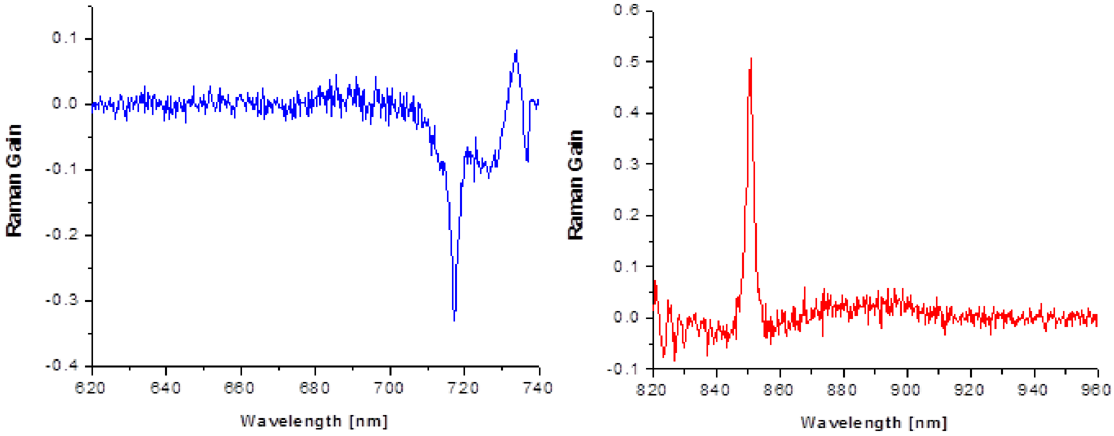

Figure 27 a) Anti-Stokes and b) Stokes SRS spectra from 3-mm calcite sample (1091 cm^{-1} mode) using broadband SRS.

In Figure 28 are two SRS spectra off of the same 3-mm calcite crystal. Each of the spectra shows simultaneous acquisition of the anti-Stokes and Stokes Raman modes. The challenges to this SRS measurement are captured in these two spectra along with those of Figure 27. When beam mode, beam alignment, pulse characteristics, pulse timing, control of nonlinear background, and collection/detection efficiencies are not optimized, there is an imbalance of the anti-Stokes and Stokes signal levels. In some cases, as in the spectra from Figure 27, only one side of the SRS spectrum is generated at a time. The source of this problem is not just a matter of timing of all of the pulses as that control is available. The cumulative effects of the factors listed above contribute to this. It should be noted that with care, a balanced SRS spectrum can be acquired as in the right spectrum in Figure 28. By implementing this version of the SRS and the analysis carried out above, there is possibility for thermometric diagnostics in thin, transparent solid materials. Without good SNR in the raw spectra and control of the background, accuracy and precision in the temperature diagnostics will be compromised.

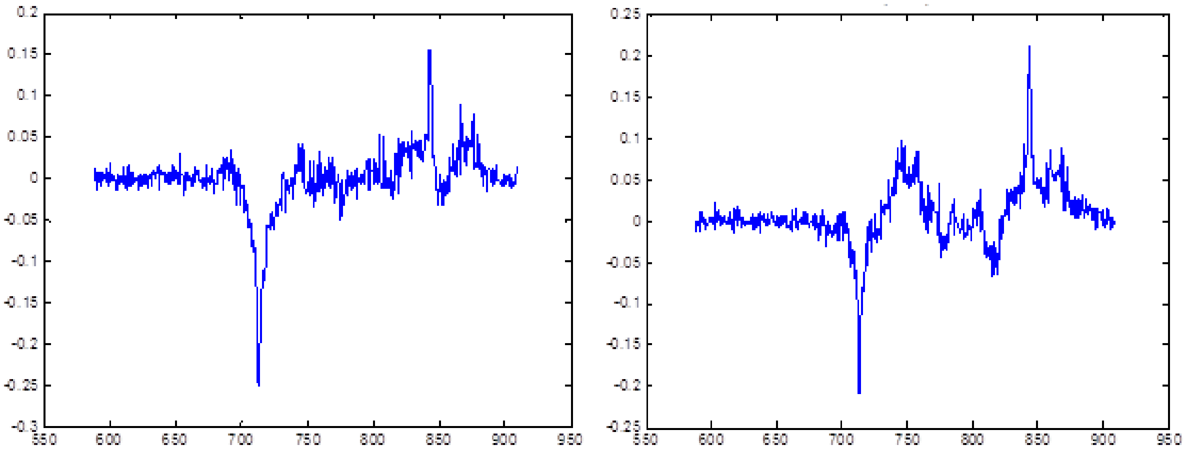

Figure 28 SRS spectra from 3-mm calcite sample (1091 cm^{-1} mode) using broadband SRS.

As an added note, an optical heterodyne detection technique was carried out to try to increase the SNR of the SRS signal. But the results showed that the rejection of the DC component of the probe spectrum did not contribute to increased SNR. Better SNR was achieved with either the direct subtraction of the pump-off probe spectrum or with the use of the reference pulse.

3.6 Conclusion

The loss-to-gain ratio in femtosecond stimulated Raman scattering can be used for temperature diagnostics in transparent, high quality solids. This method allows for access to temperature on a picosecond time scale and does not require knowledge of material parameters. Compared to spontaneous Raman scattering, the signal levels are orders of magnitude higher. But significant care must be applied to generate precise anti-Stokes and Stokes SRS signals, and samples with low SRS cross-sections require thicknesses beyond those of a thin film. Due to pump induced effects such as nonlinearities and sample burning and low cross-section for SRS, femtosecond SRS may have limited application for energetic materials if measurements require thin samples and single-shot acquisition. But, for transparent, crystalline-like materials, SRS could provide thermometric data for samples in the range of 100s of microns.

4. TRANSIENT ABSORPTION MEASUREMENT OF PETN THIN FILMS DURING LASER INDUCED SHOCK LOADING.

Two main theories of shock initiation have emerged as a result of experimental measurements and theoretical modeling. One mechanism is a thermal heating mechanism ("phonon up-pumping"), developed initially by Dlott and Fayer [22], which explains shock initiation in terms of lattice-to-molecule vibrational energy transfer. A shock wave is considered as a superposition of lattice vibrations (phonons), which couple to molecular vibrational modes via low-frequency "doorway" vibrational modes. Energy is transferred from the lattice to the vibrations of the molecule, eventually leading to bond-breaking reactions. The other postulated mechanism is a pressure-induced electronic mechanism, developed by Gilman [23, 24] and Kuklja and coworkers [25-27]. In this mechanism, uniaxial compression of the crystal lattice results in a narrowing of the electronic band gap, leading to spontaneous (athermal) decomposition reactions. Calculations show that under compression, the 5 eV band gap of an RDX crystal can be reduced to 1 eV or less under shock compression, making the ground and excited electronic states nearly degenerate and allowing instantaneous reactions to occur.

Our goal was to combine laser induced shock with a time resolved probe of electronic band gap of PETN, to determine the band gap of vapor deposited PETN shifts on the timescale of the shock rise. We completed preliminary UV transient absorption measurements on PETN thin flims under shock loading generated from the uncompressed output of an amplified Ti:Sapphire laser with no additional shaping in the spectral domain.

4.1 Experimental Setup

A "single-box" Ti: Sapphire amplifier (Spectra Physics Solstice) is utilized to provide both the shock drive pulse (uncompressed, ~150 ps FWHM, 14nm) and a compressed pulse (FWHM, 100 fs, 12 nm) for continuum generation centered at 800nm. The experimental setup of white light generation and transient absorption /laser shock measurement is shown in Figure 29. White light was generated by first doubling the compressed pulse in a BBO crystal and then focusing the 400nm output into a CaF_2 window to generate continuum extending from 400-250nm. This UV probe light was then passed through a pellicle beam splitter (Newport) and focused onto the sample with a long working distance UV objective. While a reference arm is present for shot-to-shot correction of continuum spectrum, it was blocked for preliminary measurements. Instead a series of 5 background (no light), 5 reference (UV probe only),1 shot (UV probe + shock pulse), 5 post shot (probe only) where taken of UV light illuminating PETN thin film deposed on 1.5 μm of vapor deposited aluminum [28] and used to correct shot data (Figure 30). The UV objective was placed to image sample plane (Al film surface) at spectrometer slit. Spatial calibration with standard target gave spatial resolution of 0.86um/pixel. The pump and probe spots at the sample plane were 137 and 22 um respectively. The resulting hole after shock was 267um using a 2.55 mJ pump. Lowering the rep rate of the Solstice, and then triggering two shutters, allows recovery of the single-shot absorption spectra of PETN on aluminum surface at a known delay from the shock pulse.

The UV probe was imaged to the open slit of a 0.150-m imaging spectrometer with gratings blazed at 300nm. A liquid nitrogen cooled CCD camera (Princeton UVSpec10) was directly mated to the spectrometer to provide single-shot sensitivity out to 250 nm. Transient absorption measurements were also carried out with the doubled amplifier pulse to compare to UV continuum measurements using the same procedure (Figure 30).

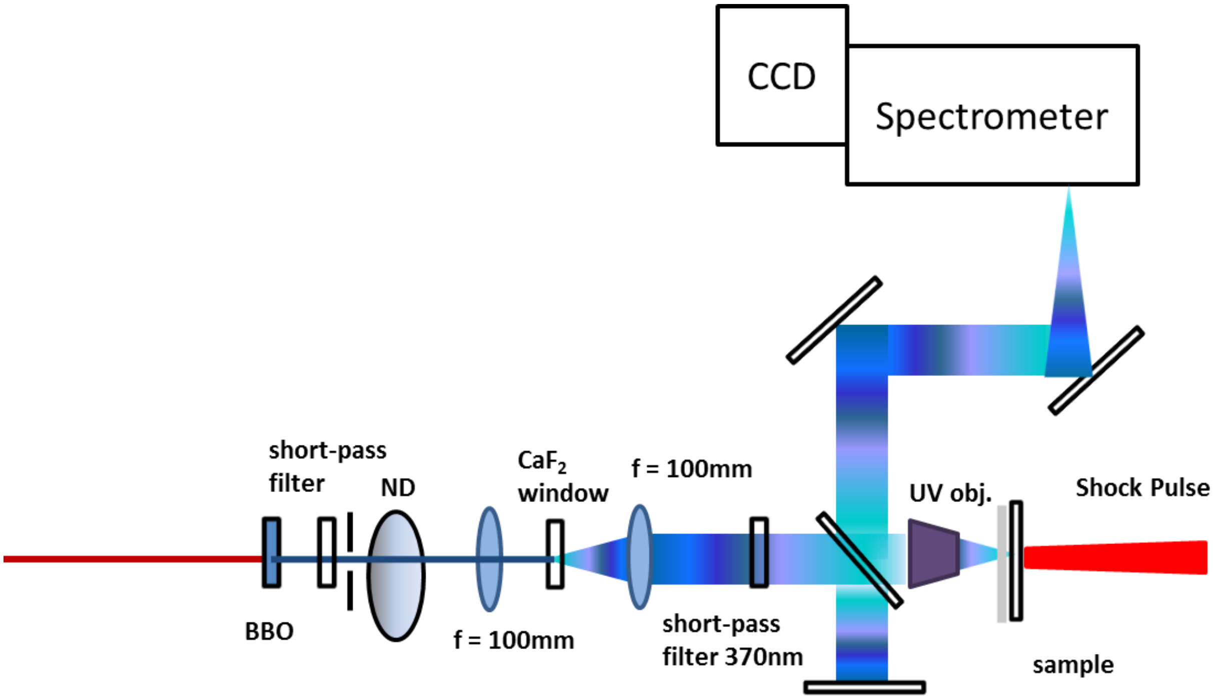

Figure 29 Schematic of transient absorption experiment. Doubled, compressed output from Ti:Sapphire amplifier is used to generate continuum in a CaF2 widow that extends into the UV (400-300 nm) . The uncompressed output of the Ti:Sapphire amplifier (Δt ~ 150 ps FWHM) is focused into an aluminum thin film to generate a shockwave that travels into the adjacent PETN thin film. Changes in the UV probe spectrum are used to follow change in the HOMO/LUMO gap of vapor deposited PETN under shock loading. Reference arm not used in preliminary measurements (blocked).

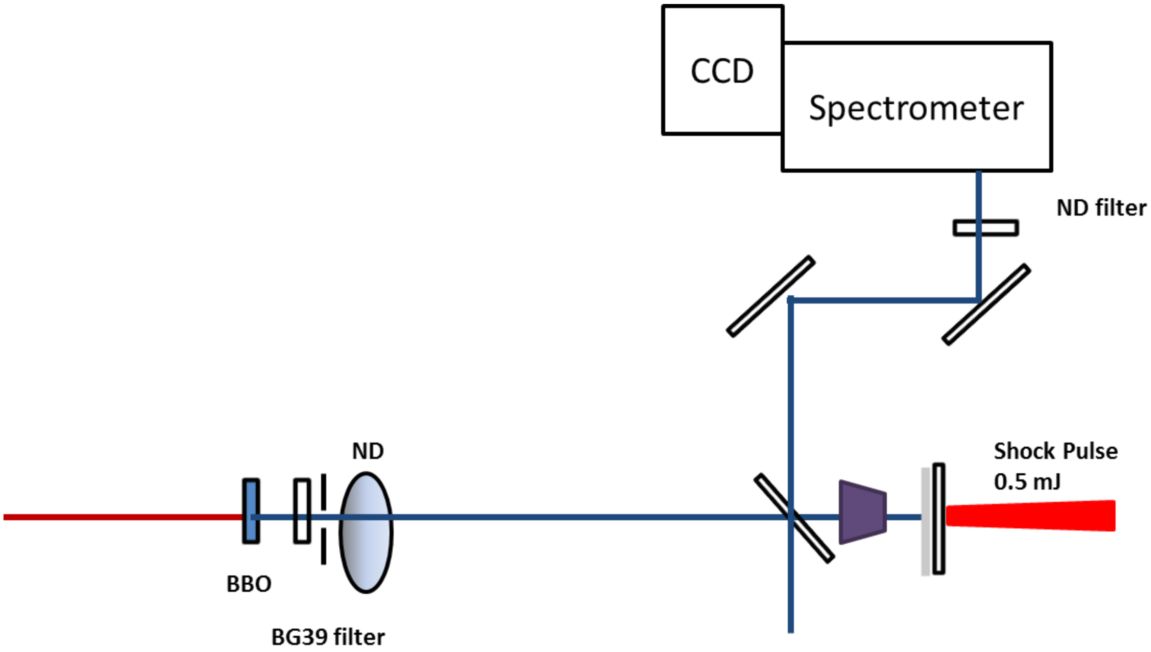

Figure 30 Schematic of transient absorption experiment using only 400nm pump (no continuum).

4.2 Results and Discussion

Results from shots on vapor deposited PETN thin films shown in Figure 31. Data were recovered from 2D images of PETN thin films with the spectrometer centered at 300 nm. Data taken for a series of delays referenced temporal overlap of pump and probe beams at sample plane as measured by a photodiode with 1 ns time resolution. Data were integrated over vertical dimension (260-320 pixels) in a region of high shock intensity, as determined from an image of breakout post shock. Intensity variations were below or near reported absorbance attributed to aluminum surface roughening in transient absorption measurements of unreactive shocked liquids in contact with an aluminum ablator [29].

Since the shot-to-shot variation in the UV continuum is significant (Figure 31), the experiment was repeated using only the 400-nm frequency-doubled laser pulse, with results shown in Figures 32-35. In Figure 32, the probe spectrum in the vicinity of 400 nm is plotted alongside the observed standard deviation in detector counts at each wavelength, revealing a more stable probe source than was observed with continuum generation. The change in the probe pulse spectrum from the PETN sample during several single-shot laser drive measurements is shown in Figure 33. Each curve represents the change in the absorption probe for the indicate time delays between the shock drive pulse and probe beam, revealing the evolution of the absorption spectrum with time during laser drive. Larger intensity drops were observed as a function of time delay (< 63% in some regions of the spectrum near 110-120 ps after the optical pump/probe overlap delay in the absence of the sample).

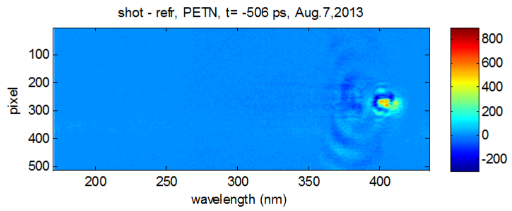
shot - refr, PETN, t= -506 ps, Aug.7,2013

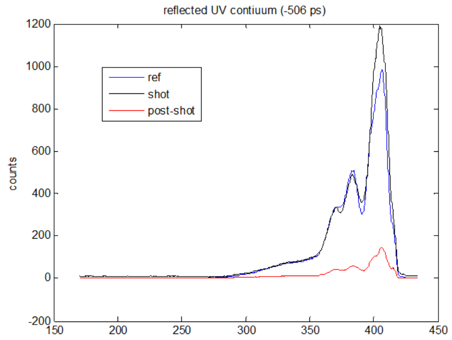
reflected UV contiuum (-506 ps)

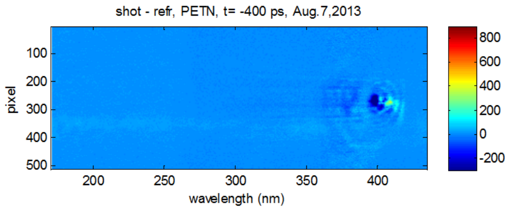
shot - refr, PETN, t= -400 ps, Aug.7,2013

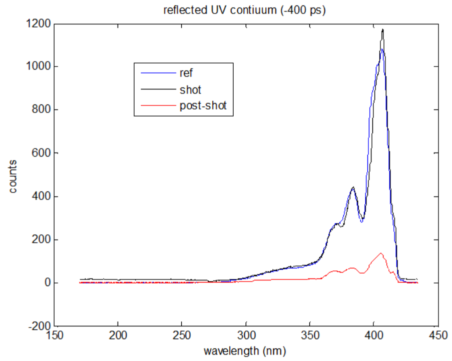
reflected UV contiuum (-400 ps)

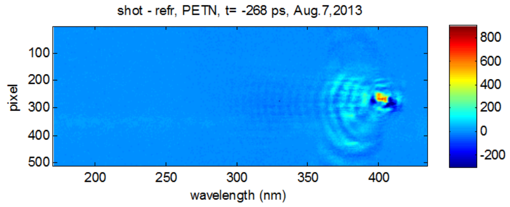
shot - refr, PETN, t= -268 ps, Aug.7,2013

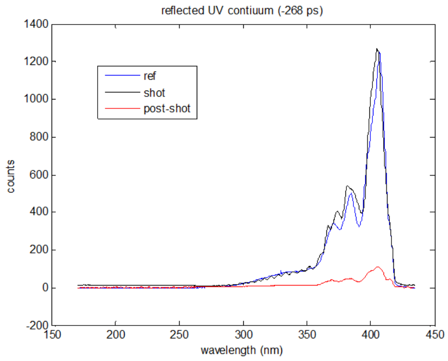
reflected UV contiuum (-268 ps)

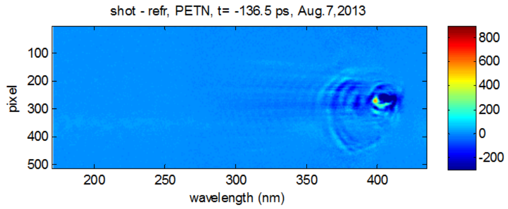
shot - refr, PETN, t= -136.5 ps, Aug.7,2013

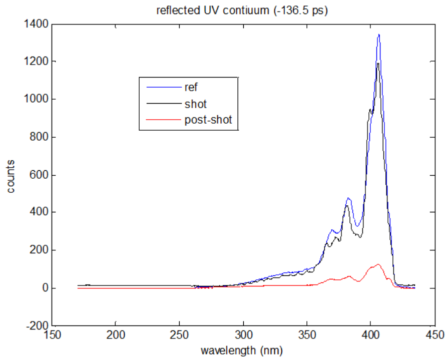
reflected UV contiuum (-136.5 ps)

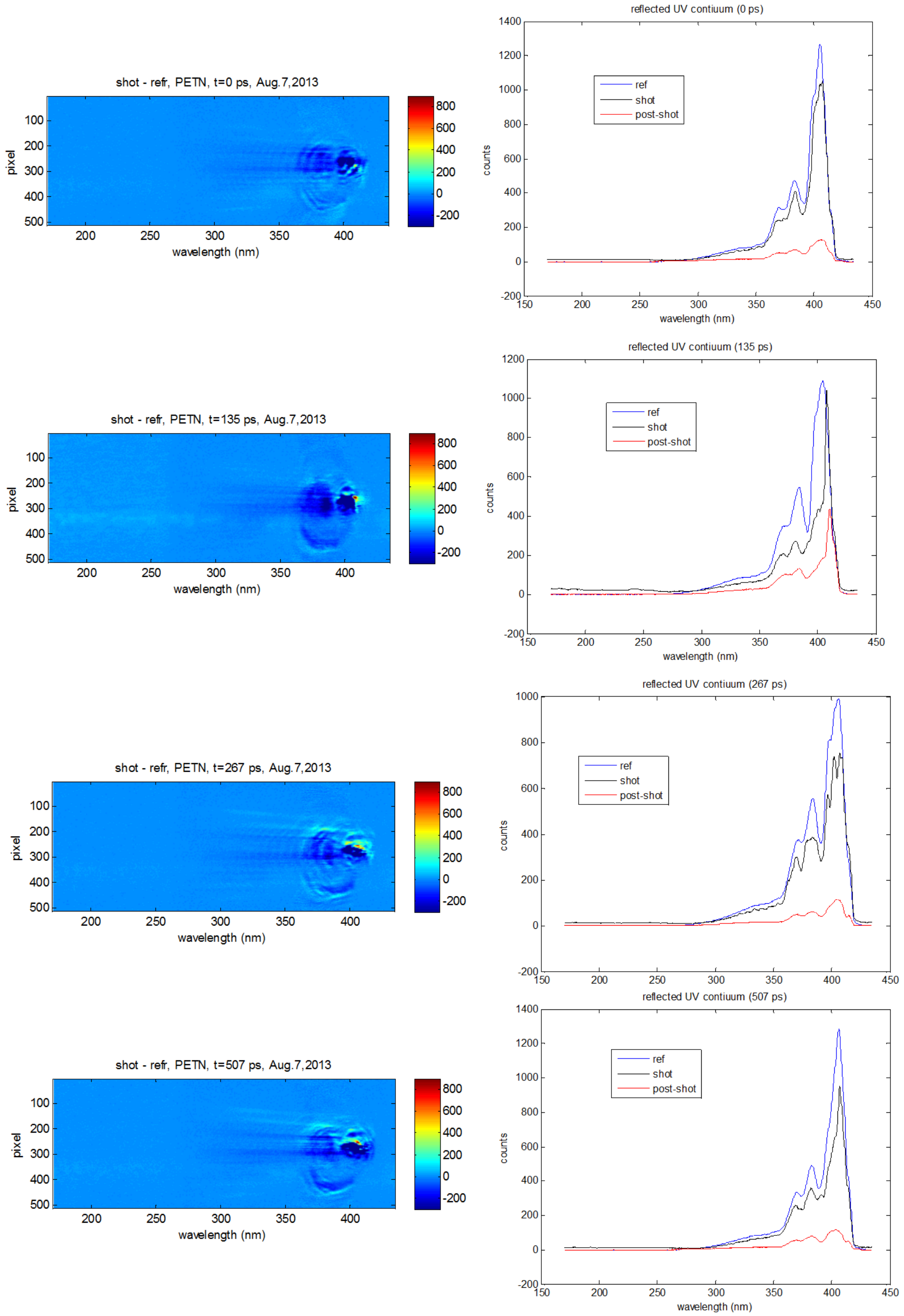

Figure 31 2D and 1D images of continuum spectrum over a series of pump/probe delays. Reference and post spectra averaged over 5 spectra.

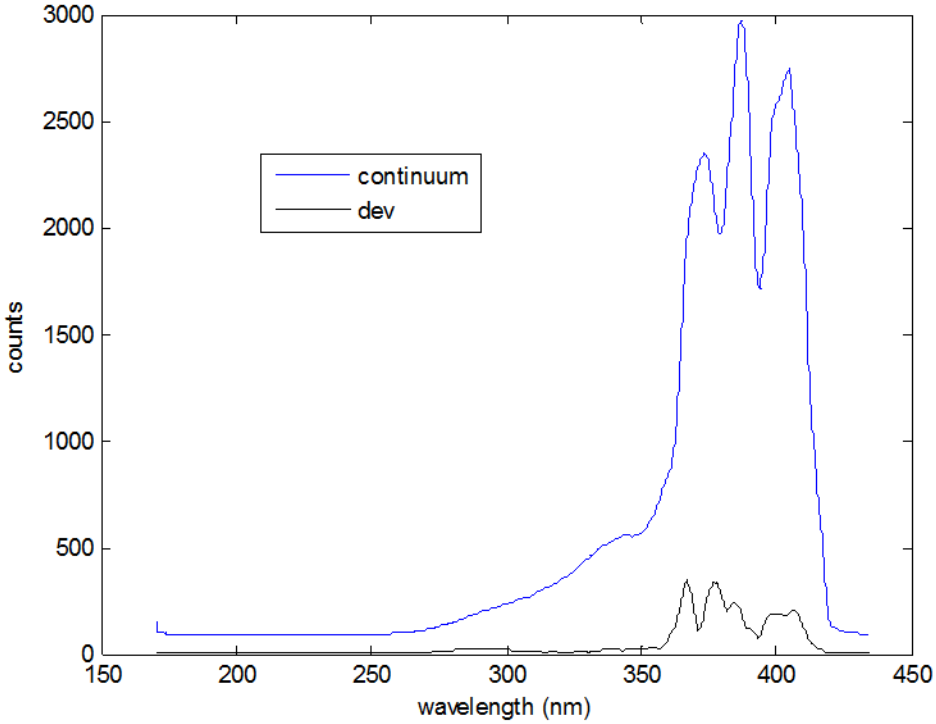

Figure 32 Average UV continuum spectrum (blue) from 40 single-shots plotted with standard deviation (black).

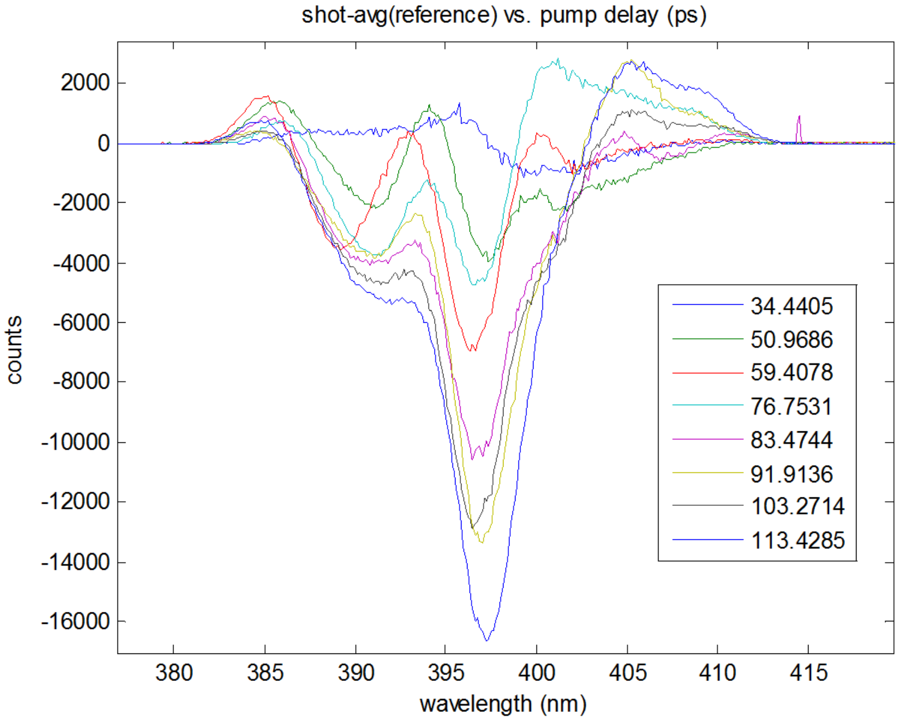

Figure 33 Intensity change of 400nm probe spectrum with pump delay (ps).

REFERENCES

1. A. Benuzzi-Mounaix, M. Koenig, J. M. Boudenne, T. A. Hall, D. Batani, F. Scianitti, A. Masini, and D. DiSanto, "Chirped Pulse Reflectivity and Frequency Domain Interferometry in Laser Driven Shock Experiments," Physical Review E **60**, R2488-R2491 (1999).
2. M. R. Armstrong, J. C. Crowhurst, S. Bastea, and J. M. Zaug, "Ultrafast Observation of Shocked States in a Precompressed Material," Journal of Applied Physics **108**, 023511 (2010).
3. C. A. Bolme, S. D. McGrane, D. S. Moore, V. H. Whitley, and D. J. Funk, "Single Shot Hugoniot of Cyclohexane Using a Spatially Resolved Laser Driven Shock Wave," Applied Physics Letters **93**, 191903 (2008).
4. M. R. Armstrong, J. C. Crowhurst, S. Bastea, W. M. Howard, and J. M. Zaug, "Prospects for Achieving High Dynamic Compression with Low Energy," Applied Physics Letters **101**, 101904 (2012).
5. M. R. Armstrong, J. C. Crowhurst, E. J. Reed, and J. M. Zaug, "Ultrafast High Strain Rate Acoustic Wave Measurements at High Static Pressure in a Diamond Anvil Cell," Applied Physics Letters **92**, 101930 (2008).
6. M. R. Armstrong, J. M. Zaug, N. Goldman, I. F. W. Kuo, J. C. Crowhurst, W. M. Howard, J. A. Carter, M. Kashgarian, J. M. Chesser, T. W. Barbee, and S. Bastea, "Ultrafast Shock Initiation of Exothermic Chemistry in Hydrogen Peroxide," Jourrnal of Physical Chemistry A **117,** 13051-13058 (2013).
7. C. A. Bolme, S. D. McGrane, D. S. Moore, and D. J. Funk, "Single Shot Measurements of Laser Driven Shock Waves Using Ultrafast Dynamic Ellipsometry," Journal of Applied Physics **102**, 033513 (2007).
8. S. D. McGrane, D. S. Moore, and D. J. Funk, "Sub-Picosecond Shock Interferometry of Transparent Thin Films," Journal of Applied Physics **93**, 5063-5068 (2003).
9. S. D. McGrane, D. S. Moore, and D. J. Funk, "Shock Induced Reaction Observed Via Ultrafast Infrared Absorption in Poly(Vinyl Nitrate) Films," Journal of Physical Chemistry A **108**, 9342-9347 (2004).
10. S. D. McGrane, D. S. Moore, D. J. Funk, and R. L. Rabie, "Spectrally Modified Chirped Pulse Generation of Sustained Shock Waves," Applied Physics Letters **80**, 3919-3921 (2002).
11. J. C. Crowhurst, M. R. Armstrong, K. B. Knight, J. M. Zaug, and E. M. Behymer, "Invariance of the Dissipative Action at Ultrahigh Strain Rates above the Strong Shock Threshold," Physical Review Letters **107**, 144302 (2011).
12. V. H. Whitley, S. D. McGrane, D. E. Eakins, C. A. Bolme, D. S. Moore, and J. F. Bingert, "The Elastic-Plastic Response of Aluminum Films to Ultrafast Laser-Generated Shocks," Journal of Applied Physics **109**, 013505 (2011).
13. S. P. Marsh, *LASL Shock Hugoniot Data* (University of California Press, 1980).
14. M. R. Armstrong, Unpublished Data, Lawrence Livermore National Laboratory (2014).
15. R. Knepper, K. Browning, R. R. Wixom, A. S. Tappan, M. A. Rodriguez, and M. K. Alam, "Microstructure Evolution During Crystallization of Vapor-Deposited Hexanitroazobenzene Films," Propellants, Explosives, and Pyrotechnics **37**, 459-467 (2012).

16. W. C. McCrone, "Crystallographic Study of Hexanitroazobenzene (HNAB)", SAND75-7067, Sandia National Laboratories (1975).
17. E. J. Graeber, and B. Morosin, "The Crystal Structures of 2,2',4,4',6,6'-Hexanitroazobenzene (HNAB), Forms I and Ii," Acta Crystallographica **B30**, 310-317 (1974).
18. S. Roy, J. R. Gord, and A. K. Patnaik, "Recent Advances in Coherent Anti-Stokes Raman Scattering Spectroscopy: Fundamental Developments and Applications in Reacting Flows," Progress in Energy and Combustion Science **36**, 280-306 (2010).
19. N. C. Dang, C. A. Bolme, D. S. Moore, and S. D. McGrane, "Femtosecond Stimulated Raman Scattering Picosecond Molecular Thermometry in Condensed Phases," Physical Review Letters **107**, 043001 (2011).
20. N. C. Dang, C. A. Bolme, D. S. Moore, and S. D. McGrane, "Temperature Measurements in Condensed Phases Using Non-Resonant Femtosecond Stimulated Raman Scattering," Journal of Raman Spectrscopy **44**, 433-439 (2012).
21. S. M. Shapiro, D. C. O'Shea, and H. Z. Cummins, "Raman Scattering Study of the Aplpha-Beta Phase Transition in Quartz," Physical Review Letters **19**, 361-364 (1967).
22. D. D. Dlott, and M. D. Fayer, "Vibrational up Pumping, Defect Hot Spot Formation, and the Onset of Chemistry," Journal of Chemical Physics **92**, 3798-3812 (1990).
23. J. J. Gilman, "Chemical Reactions at Detonation Fronts," Philosophical Magazine B **71**, 1057-1068 (1995).
24. J. J. Gilman, "Mechanochemistry," Science **274**, 5284 (1996).
25. M. M. Kuklja, "Role of Electronic Excitations in Explosive Decomposition of Solids," Journal of Applied Physics **89**, 4156-4166 (2001).
26. M. M. Kuklja, "On the Initiation of Chemical Reactions by Electronic Excitations in Molecular Solids," Applied Physics A **76**, 359-366 (2003).
27. M. M. Kuklja, E. V. Stefanovich, and A. B. Kunz, "An Excitonic Mechanism of Detonation Initiation in Explosives," Journal of Chemical Physics **112**, 3417-3423 (2000).
28. R. Knepper, "Controlling the Microstructure of Vapor-Deposited Pentaerythritol," Journal of Materials Research **26**, 1605-1613 (2011).
29. N. C. Dang, C. A. Bolme, D. S. Moore, and S. D. McGrane, "Shock Induced Chemistry in Liquids Studied with Ultrafast Dynamic Ellipsometry and Visible Transient Absorption Spectroscopy," Journal of Physical Chemistry A **116**, 10301-10309 (2012).

DISTRIBUTION (sent electronically)

1	MS1454	D.A. Farrow	02554
1	MS1454	B.A. Jilek	02554
1	MS1454	R. Knepper	02554
1	MS1454	I.T. Kohl	02554
1	MS1454	L.M.G. Minier	02554
1	MS1454	A.S. Tappan	02554
1	MS1454	W.M. Trott	02554
1	MS1454	R.R. Wixom	02554
1	MS1453	J.L. Moya	02550
1	MS1190	C.J. Bourdon	01675
1	MS1153	J. Urayama	05444
1	MS0828	T.L. Durbin	01512
1	MS0826	S.P. Kearney	01512
1	MS0359	D.L. Chavez, LDRD Office	07911
1	MS0899	Technical Library	09536 (electronic copy)

Sandia National Laboratories